Insight Into Frontal Seismogenic Zone in the Mentawai Locked Region From Seismic Full Waveform Inversion of Ultralong Offset Streamer Data

Yanfang Qin, Satish C. Singh

AGU100 ADVANCING EARTH AND SPACE SCIENCE

Geochemistry, Geophysics, Geosystems

RESEARCH ARTICLE
10.1029/2018GC007787

Key Points:
- Elastic full waveform inversion is applied to long streamer data at the subduction front in the Mentawai locked zone
- Combination of downward extrapolation data and surface streamer data following the frequency continuation strategy is efficient during inversion
- Active frontal thrusts and low-velocity décollement at the plate interface relate to tsunami earthquake

Supporting Information:
- Supporting Information S1

Correspondence to:
Y. Qin,
qin@ipgp.fr

Citation:
Qin, Y., & Singh, S. C. (2018). Insight into frontal seismogenic zone in the Mentawai locked region from seismic full waveform inversion of ultralong offset streamer data. *Geochemistry, Geophysics, Geosystems*, *19*, 4342–4365. https://doi.org/10.1029/2018GC007787

Received 29 JUN 2018
Accepted 17 OCT 2018
Accepted article online 24 OCT 2018
Published online 8 NOV 2018

Insight Into Frontal Seismogenic Zone in the Mentawai Locked Region From Seismic Full Waveform Inversion of Ultralong Offset Streamer Data

Yanfang Qin[1] **and Satish C. Singh**[1,2]

[1]Equipe de Géosciences Marines, Institut de Physique du Globe de Paris (CNRS, Paris Diderot, Sorbonne Paris Cité), Paris, France, [2]Earth Observatory of Singapore, Nanyang Technological University, Singapore

Abstract Sumatra subduction zone is one of the most seismically active zones on Earth. After having produced three $Mw > 8.4$ earthquakes and several $Mw > 7.5$ earthquakes, including the $Mw = 7.8$ 2010 tsunami earthquake, the northern Mentawai segment is still locked and is capable of generating a great earthquake, possibly a disastrous tsunami. We analyzed ultralong offset seismic reflection data from this locked zone to characterize the nature of the accretionary prism and the plate interface using a combination of traveltime tomography, full waveform inversion, and prestack depth migration. In order to enhance the refractions, we downward extrapolate the streamer data to the seafloor, allowing the refraction arrivals to be observed from near-zero offset up to far offset, and use a traveltime tomography to determine the background velocity in the upper sediments. Starting from these velocities, we perform a multiscale elastic full waveform inversion to determine the detailed *P* wave velocity structure of the subsurface. Based on this velocity, we perform a prestack depth migration to obtain seismic image in the depth domain and compute the porosity of the sediments to determine fluid content along faults. Our results show a low-velocity subduction channel with high porosity at the plate interface that connects the likely active frontal thrusts at the toe of accretionary wedge, suggesting that the frontal section of the prism is seismogenic. We have also observed a low-velocity layer in the middle of wedge separating old sediments below from new sediments above, defining the roots of bivergent thrust faults up to the seafloor, which can be interpreted as a psudo-décollement.

1. Introduction

Sumatra subduction is one of the most active subduction zones in the world. Here the Indo-Australian plate subducts beneath the Eurasian (Sunda) plate obliquely, where the obliquity increase northwestward (Figure 1a). The convergence in the south near Java is nearly orthogonal to the trench with a convergence rate of 67 mm/year (Tregoning et al., 1994). It starts becoming oblique at Sunda Strait and turns nearly arc parallel near Andaman Islands in the north, with the convergence varying from 60 to 43 mm/year (Gahalaut et al., 2006; Prawirodirdjo & Bock, 2004; Figure S1 in the supporting information). Starting from the 26 December 2004 $Mw = 9.2$ Sumatra-Andaman earthquake, which caused a devastating tsunami with the water runup height of 30 m (Geist et al., 2006; Lay et al., 2005), the Sumatra subduction zone has experienced many large megathrust earthquakes with $Mw > 7.5$. These earthquakes nucleated on the interface between the subducting plate and the overriding plate, rupturing from the seafloor down to 30–40 km below the forearc (Singh et al., 2008). The rupture of the 2004 earthquake reached the subduction front, caused uplift of water column and produced the large tsunami (e.g., Ammon et al., 2005; Gulick et al., 2011; Kerr, 2005; Singh et al., 2008). After 3 months in March of 2005, there was another event with a magnitude of 8.7 off the western coast of Sumatra between Nias and Simeulue Islands, broke 350 km of the plate boundary (Briggs et al., 2006) without generating a large tsunami; the slip terminated updip of the maximum rupture patch underneath the Simeulue and Nias forearc islands (Konca et al., 2008). Two years later in 2007, twin earthquakes occurred along the southern Mentawai Island with $Mw = 8.4$ and $Mw = 7.9$, breaking 200 km of the plate boundary and leaving a gap of ~600 km between the 2005 and 2007 events (Konca et al., 2008); these events also did not produce any large tsunami. In October 2010, another tsunami earthquake of $Mw = 7.8$ occurred at the southwest corner of Pagai Island, which ruptured the frontal section of the 2007 earthquake, producing a tsunami with water runup height of 8 m on SW coast of Pagai Island (Hill et al., 2012; Lay et al., 2011; Singh, Hananto, Mukti Permana et al., 2011). After having produced so many large

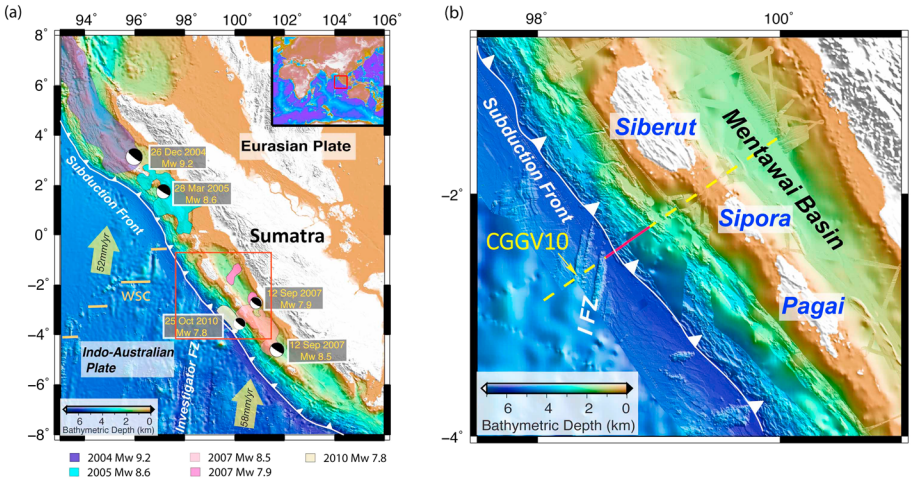

Figure 1. (a) Study area where five big earthquakes with $Mw > 7.5$ occurred during the last decade. WSC is the Wharton Spreading Center; the subduction rates and directions are marked by yellow arrows; the white line indicates the subduction front; colored patches delimit areas of main slip of these five earthquakes (Feng et al., 2015); the red box marks the area in panel b. Insert at the upper right indicates the location of the study area. (b) A blowup of the Mentawai segment. Seismic profile CGGV10 is marked by yellow dashed line, where the red solid line indicates the part of data used in this study. IFZ indicates Investigator Fracture Zone. The high-resolution bathymetric data are from Ladage et al. (2006).

earthquakes, the northern Mentawai zone is still locked with a downdip edge at ~55 km (Chlieh et al., 2008; Konca et al., 2008). Although the geodetic and paleogeodetic measurements could not provide tight constraints on the shallowest portion of megathrust (Chlieh et al., 2008), the temperature modeling of the plate interface does not show particular patterns and indicates that the locked status may extend to the trench; this is further confirmed by the 2010 tsunami earthquake. Thus, this area is capable of generating a great earthquake in the near future, possibly with rupturing up to the subdcution front and producing a disastrous tsunami, similar to the last megathrust earthquake that ruptured in this region in 1833 (e.g., Natawidjaja et al., 2006). And, therefore, it is extremely important to study this section of the subduction front.

The nature of coupling at the plate interface could be influenced by heterogeneities in the seismogenic locked zone (Aki, 1979), which can be due to the existence of seamounts (e.g., Kodaira et al., 2000; Park et al., 1999; Singh, Hananto, Mukti, Robinson et al., 2011), ridges, fracture zones (Fuller et al., 2006), broken subducting plate (Singh et al., 2008), or hydration of the slab (Shillington et al., 2015). The irregular subducting plate geometry on the plate interface can produce lateral discontinuities that can act as a barrier to the lateral propagation of coseismic rupture and reduce the maximum size of an earthquake (Kodaira et al., 2000; Singh, Hananto, Mukti, Robinson, et al., 2011), or it also can work as an asperity during an earthquake (e.g., Husen et al., 2002). Therefore, it is important to characterize the nature of the plate interface and accretionary prism to understand the frontal locking, rupturing, and tsunami generation, including physical, geomechanical, thermal, and hydrological properties of the plate interface. Controlled source seismic experiments are good ways to investigate these characters, and to estimate physical properties of subduction zones such as seismic wave velocities, porosity, and pore pressure (Bangs et al., 1990; Calahorrano et al., 2008; Kamei et al., 2012; Kodaira et al., 2004).

In order to mitigate the seismic and tsunami risk, CGG, an integrated geoscience company, acquired deep seismic reflection data in the Mentawai locked zone in the 2007 earthquake rupture zone and in the aseismic zone using a 15-km-long streamer and a powerful air gun source (Singh et al., 2009). Here we analyze one part of these ultralong offset seismic reflection data at the frontal section of the Mentawai locked zone to characterize the nature of the accretionary prism and the plate interface using a combination of 2-D traveltime tomography, full waveform inversion (FWI), and prestack depth migration (PSDM) to shed light upon the nature of this patch.

2. Study Area

Our study area is located in the Mentawai highly coupled zone (Figure 1) (Chlieh et al., 2008), offshore central Sumatra, south of Siberut Island. The age of subducting oceanic crust is 64–65 Ma (Jacob et al., 2014). At the

southwestern side of Siberut Island, the Investigator Fracture Zone subducts beneath the trench along a N7°E oriented trend in a 105-km-wide zone and forms an ~40° intersection angle with the subduction front; near the trench, it separates 48-Ma old oceanic crust in the west from the 65-Ma old oceanic crust in the east (Jacob et al., 2014; Liu et al., 1983). The uplift and deformation in the subduction front offshore of Mentawai seems to be related to the subducting Investigator Fracture Zone and other complex bathymetric highs on the oceanic plate (e.g., Bilek et al., 2003; Dominguez et al., 2000). The Investigator Ridge (IR) and further north the fossil Wharton Spreading Ridge act as barriers that stop the Bengal-Nicobar fan sediments moving toward south, so the sedimentary layer in the Mentawai zone is thin at the trench (Figure S2). Lower parts of the sediments in the Mentawai zone are pelagic, followed by recent trench-filled sediments (Singh, Hananto, Mukti, Permana, et al., 2011). The dip of the subducting plate is ~7.5°at the depth of 12 km, which increases to ~12°at 110 km landward from the trench axis (Singh, Hananto, Mukti, Permana, et al., 2011). From the subduction front (toe of accretionary prism) up to the accretionary wedge, there are many anticlinal ridges, similar to northern Sumatra (e.g., Ghosal et al., 2014). The thickness of sediments increases toward landward along the accretionary prism. Here we seek to determine the high-resolution *P* wave velocity structure of the frontal section in the Mentawai locked region. We will focus on a 40-km portion along profile CGGV10 that covers ~5 km of the oceanic basin, the deformation front and ~35 km of the accretionary prism (Figures 1b and S2).

3. Data Acquisition

The 2-D seismic reflection profile CGGV10 (Figure 1b) was acquired by CGGVeritas (now called CGG) in May 2009 on board of the seismic vessel Geowave Champion. This profile is 240 km long and traverses the whole subduction system, starting from the IR and crosses the subducting oceanic plate on the Indo-Australia plate, subduction front, accretionary wedge, forearc high, and the Mentawai forearc basin. An array of 48 air guns with a total volume of 158 L was deployed at 15-m water depth providing a very powerful low-frequency energy source required to image deep targets. The shot spacing was 50 m, and the record length was 20 s. A 15-km-long streamer with a 12.5-m receiver group interval was towed at 22.5-m water depth. The data were resampled to 4 ms and processed using an antialias filter high cut at 90 Hz. The vessel moved at a speed of 4–4.5 kn. Since the source was towed at water depth of 15 m and the streamer was at 22.5 m, the data contain rich low frequencies and is appropriate for FWI.

4. Downward Continuation

The water depth in our study area varies from 5.5 to 2.5 km (Figure S3a). This thick water layer makes the refraction wave to be observed only at the limited far offset of the shot gathers (Figure S3b), which limits the application of conventional first arrival tomography. At the same time the steep slope and complex topography cause strong 3-D scattering effects (Figure S3b), making it difficult to estimate velocity using conventional normal moveout velocity analysis. This 3-D scattering noise cannot be simulated by 2-D wave propagation modeling, so this noise also poses difficulties in the waveform inversion. In order to overcome these limitations of conventional analysis methods, we apply redatuming method and extrapolate both shots and receivers from the sea surface to sea bottom by using Kirchhoff integral extrapolation technique in the time domain (Arnulf et al., 2011, 2014; Berryhill, 1979, 1984; Ghosal et al., 2014).

The original multichannel seismic data contain a strong swell noise. Our preprocessing of original data was kept to a minimum only with two minimum phase Butterworth filters low cut at 1 Hz with 8 dB per octave increasing to 2 Hz with 12 dB per octave, and high cut at 42 Hz, providing a clean broadband signal with lowest frequency < 2 Hz. To reduce the computing costs, we decimated the data to 8 ms of sample rate. We estimated the water velocity using normal move out velocity method at the flat region, which is ~1,485 m/s. The water depth had been obtained by12-kHz transducer echo sounder and ships navigational echo sounder. First, the downward continuation (DC) was performed in the common shot gather to extrapolate all the receivers to the seafloor, then after sorting the results into common receivers, the DC was applied to extrapolate the shots to the seafloor. In order to avoid aliasing due to the difference between the shot interval (50 m) and receiver interval (12.5 m), the data were interpolated during the DC process. Finally, the data were resorted into the shot domain (Berryhill, 1984).

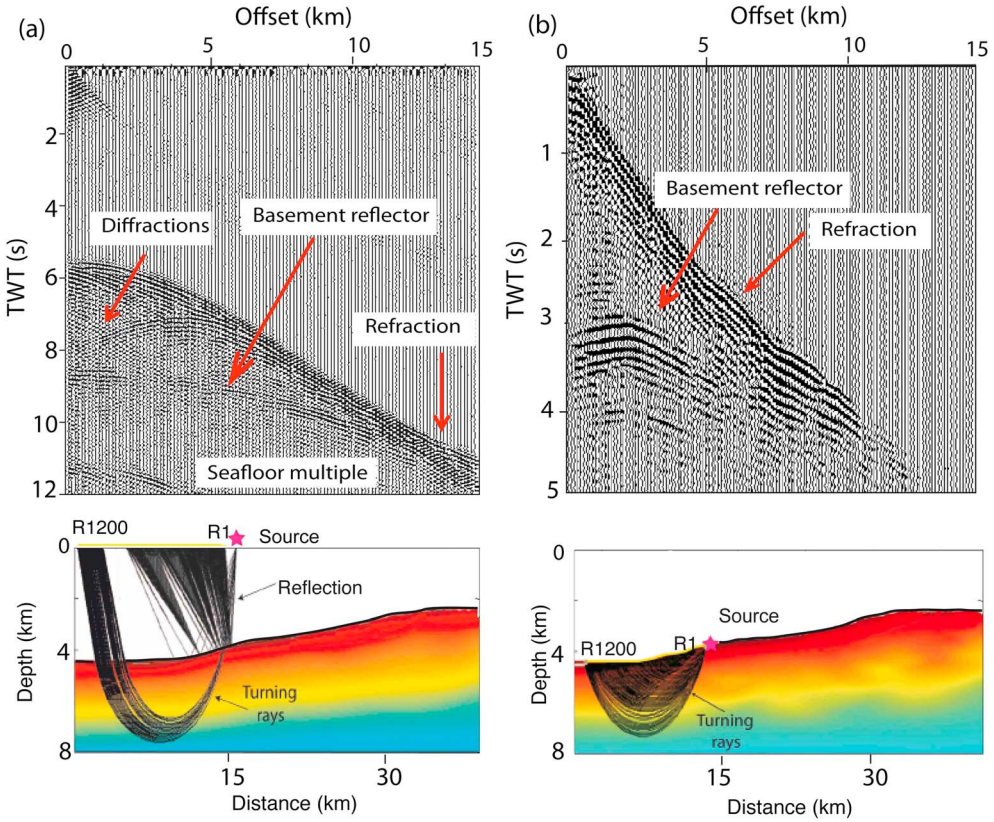

Figure 2. (a) A surface streamer seismic shot gather (top) and its corresponding ray diagram (bottom). (b) The shot gather in panel (a) after downward extrapolated source and receivers to the seafloor showing refraction as first arrivals from near to far offsets (top) and the corresponding ray diagram (bottom). TWT = Two way travel time.

Figure 2 shows one of the shot gather before and after the DC process, and their associated seismic raypaths. The early arrivals in the surface streamer data (Figure 2a) are dominated by the shallow sediment reflections and diffractions, only the far offset part (12–15 km) contains refractions, hence turning rays only cover a limited part of the model. The DC has collapsed the seafloor diffractions and has brought out refractions from shallow structures as first arrivals, from nearly zero offset to far offset by collapsing the seafloor reflection toward a point at zero offset, leading to a higher ray coverage of the turning rays in the upper part of the model (Figure 2b). This helps us to obtain traveltime picks for rays traveling through the shallow part of the model and provides better quality data for waveform inversion. DC data are also helpful in reducing the computation cost, the model size is reduced by removing 2 km topmost water layer and the recording time changed from 10 to 5 s.

However, the DC data contains strong artifacts at far offset, because of the boundary effect that caused by the limited length of the offset. By comparing the synthetic forward modeling data with the DC data, we found that the amplitude of wavelets is reliable in the first three quarters of the whole offset, which means the data within offset $<$11.25 km can be used for the waveform inversion. On the other hand, artifacts also had been generated in the near offset, which come before the first arrivals. These noisy signals are mixed with the first arrivals and bring difficulties to the first arrivals picking. So during the traveltime tomography, we exclude the nearest 3 km of offset. Although the amplitudes and phases of the data are well preserved as the geometrical spreading has been taken into account during DC process, direct waves and the effect of free surface on source and receiver sides are not included. Furthermore, if a powerful source is placed on seafloor, the surface wave would be generated during the forward waveform modeling, but the downward continued data would not have those surface waves and one has to take them into consideration during the waveform inversion.

Starting from the DC data, we apply traveltime tomography and FWI to gradually constrain the model from long to small scales, followed by reflection waveform inversion based on original streamer data to address the fine scale features and complete the whole *P* wave velocity model estimation, using both frequency and offset multiscale strategies.

5. Traveltime Tomography

For traveltime tomography, the surface multichannel seismic data were downward extrapolated to a slightly smoothed seafloor (Figure S3a). Although this would introduce small errors in the traveltime computation, it would overcome the discontinuity from trace to trace after DC due to the sharp variations of the topography.

Traveltimes of first arrival refractions were picked for 439 shots that had been decimated at 100-m shot interval along the line. The first breaks were picked by using cross correlation technique and corrected manually. Because of the artifacts caused by the DC in the near and far offsets, we only picked the first arrivals in the range of offset from 3 to 11.25 km in each shot gather. We picked traveltimes at every fourth receiver with an interval of 50 m. The total shot number is 439, providing 72,874 traveltime picks. An uncertainty of 25 ms was assigned to each pick. This is based on our estimation of uncertainty associated with the smoothed bathymetry that is slightly different from the actual bathymetry of an average ~20 ms, shot and receiver positions of 2 ms, and the picking uncertainty of 8 ms.

The tomography algorithm we used is developed by Van Avendonk et al. (2004), in which the seismic wave traveltime was computed by the shortest path method (Moser, 1991). The whole model for computing is 62 km long and 11 km deep. We parameterized $u_0(x,z)$ (slowness model) with a horizontal grid spacing of 100 m and a vertical grid spacing of 50 m. After eight iterations of inversion, we decreased the grid size to a half. For tomography algorithm stability testing, we used two different starting models (1-D linearly increased velocity model and smoothed stacking velocity model) and performed the same number of iterations, and both of them gave similar results (see supporting information Figure S4).

As the first arrivals have limited depth coverage, we used the smoothed and interpolated stacking velocity as the starting model for traveltime tomography (Figure 3a) in order to make sure that we have some constrains in the deep domain (below turning rays). We carried out the inversions followed by ray tracing in the updated model iteratively. The ray coverage, which indicates the sensitivity of tomography, is down to ~3 km below the seafloor. In theory, iterations are performed to fit the data until smoothing constraints are satisfied and an overall chi-square misfit value (the sum of the squared individual traveltime misfits divided by the overall assigned uncertainty) reduced to ~1.0. The misfit between the observed and calculated traveltime is minimized in a least square sense. Reduction in the traveltime misfits are monitored by observing the chi-square value, which was 20 before the inversion and reduced to 1.5 after 11 iterations, indicating that the traveltime residuals were similar in the size to the predefined data errors. We stopped here instead of continuing the inversion to let chi-square approach 1.0 and over fitting the model, which could be due to the errors of the traveltime picks on the phase interpretation, and the inaccuracy caused by ray tracing assumptions such as ray bending effects (Van Avendonk et al., 2004). During the inversion, we employed a roughness matrix that contains both first (flatness) and second (smoothness) derivatives with equal weight to regularize the inversion (e.g., Zelt et al., 1999; Zhang & Toksöz, 1998). Horizontal derivatives were given a weight 3 times larger than vertical derivatives to account for the fact that the seismic velocity structure is likely to be rougher in the vertical direction.

The inverted result contains long-wavelength velocity structures (Figure 3b). In the ray-covered region, the high-velocity layer ($>$4 km/s) close to the seafloor starts from ~6 km of depth in the trench (distance range $<$ 0 km), while the velocity just below the seafloor at the toe of the accretionary prism (distance range 0–5 km) is low (~1.7 km/s). The velocity contours follow the shape of the anticlinal ridges moving up to the accretionary wedge. Below the ray-covered region, the velocity constraints are still poor.

The traveltime root-mean-square misfit has significantly decreased after the inversion (Figure 4). We notice that the residuals do not change as much as other places in the trench area ($-$7–0 km), which is probably because the presence of the IR on the SW side (Figure S2) results in strong artifacts in the DC gathers leading to poor picks and poor convergence (Figure S5), or the inversion also has some difficulties in resolving the very thin low-velocity top layer above very high velocity material at the same time (Henig et al., 2012).

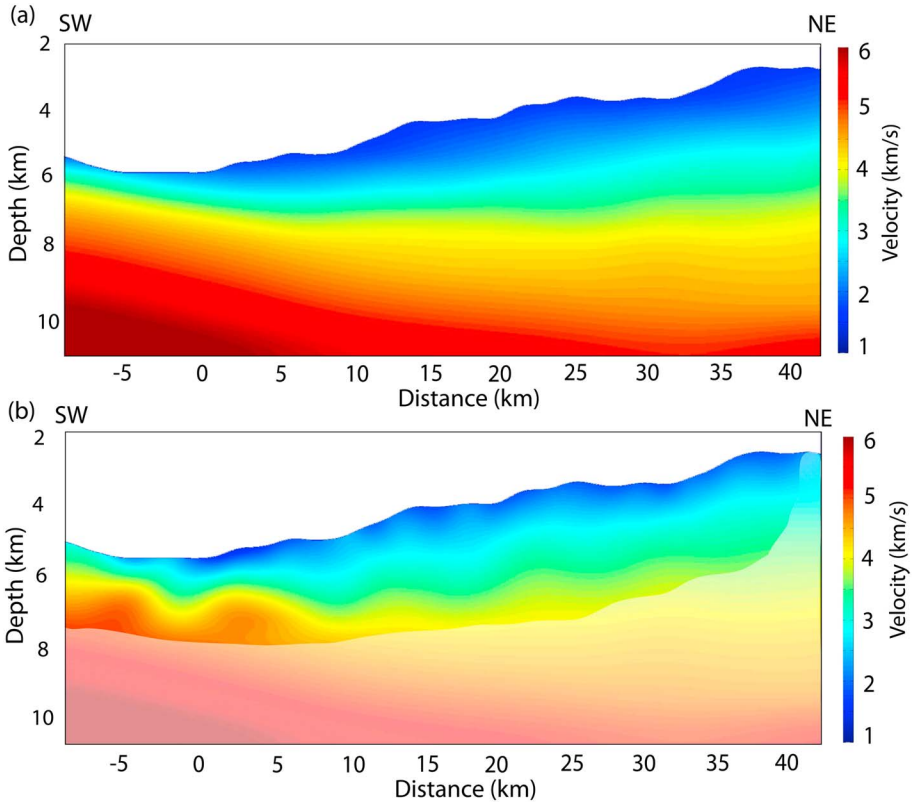

Figure 3. (a) Starting model for ray-based first arrival tomography. (b) Inverted first arrival tomography velocity model. The shadowed zone represents the area with no ray coverage.

Before the inversion, the distribution of data misfit is asymmetric, but it approaches to a Gaussian after the inversion, with the mean at zero suggesting that the inversion scheme has produced an unbiased model (Figure S6). To assess our results are reliable, we carried out checkerboard tests (Figure S7; for details see supporting information; Hearn & Ni, 1994; Zelt et al., 1996; Zelt, 1998), which indicates that we can resolve the feature with a minimum size of 500 m down to ~3 km below seafloor and the resolution of the topmost 2 km is robust enough.

6. FWI

FWI is a powerful tool to extract the subsurface quantitative information from seismic data (Lailly, 1983; Tarantola, 1984). The FWI algorithm we implement is based on the work of Shipp and Singh (2002) on the basis of the theoretical frameworks for elastic inversion of Tarantola (1984, 1986) and Mora (1987). The FWI

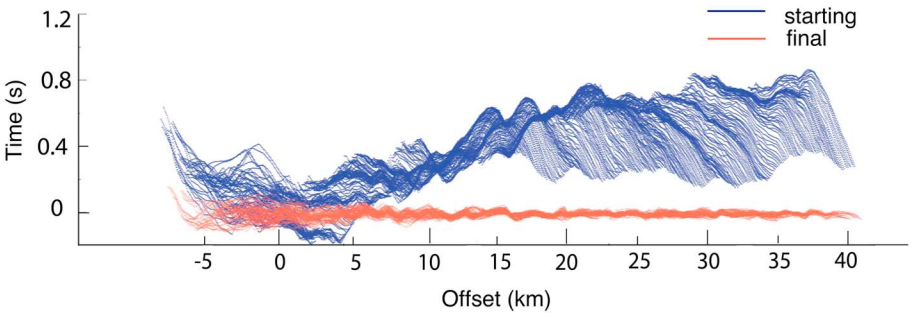

Figure 4. Traveltime misfit versus source-receiver offsets in the global model scale: Starting misfit (blue) and final misfit (red).

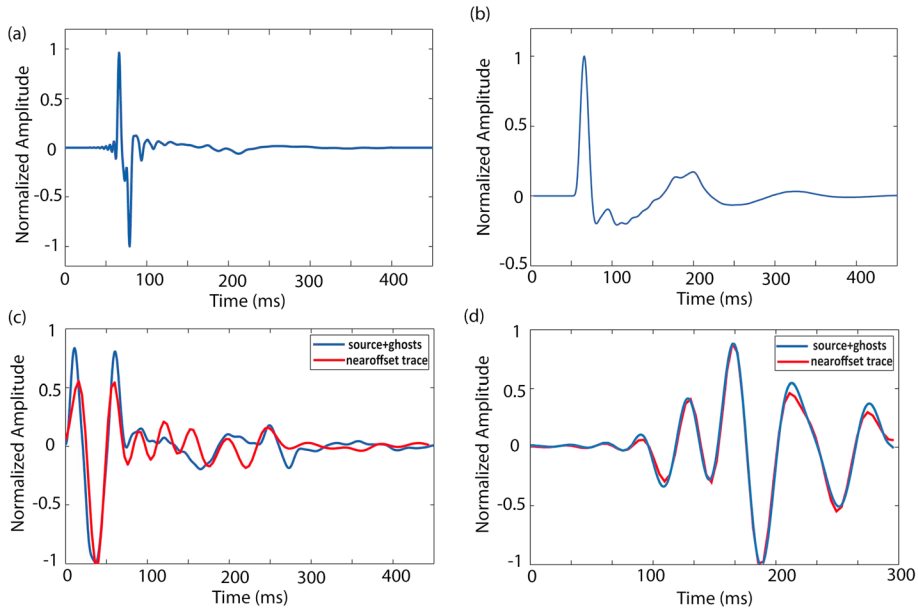

Figure 5. (a) Original far-field source. (b) Deghosted source. (c) The comparison between the minimum phase reconstructed near offset data and the source wavelet obtained without spectrum filtering. Red curves are the stacked near-offset data and cut off the first reflector; blue curves are the deghosted source incorporated synthetic source and receiver ghosts. (d) The comparison of the same wavelets as in (c) but after Wiener shaping filtering, which will be the input source for full waveform inversion.

attempts to iteratively minimize the misfit function between the observed and synthetic seismic waveform data in a least squares sense. The least squares misfit function requires the observed data to have high signal-to-noise ratio (Igel et al., 1996; Shipp & Singh, 2002), so before performing the inversion, a preprocessing procedure is always needed. On the other hand, to avoid the misfit function converging into local minimum, a good starting velocity model is required, which should be close enough to the true model (e.g., Virieux & Operto, 2009). Here we use the tomography result that contains long wavelength features of the true velocity model as a starting model for the *P* wave. The starting *S* wave velocity is obtained by using the empirical relationships that is linked to the *P* wave velocity primarily by the findings of Castagna et al. (1985) for low values and Fliedner et al. (1998) for the higher *P* wave velocities greater than 3.5 km/s. The density is linked to the *P* wave velocity by the empirical relationship that is based on the Hamilton (1978) formula for the *P* wave velocity below 2.2 km/s, and according to Gardner et al. (1974) relationship for the higher *P* wave velocity.

6.1. Source Estimation

FWI result is very sensitive to the source signature. Source signature is directly related to the subsurface structures and any redundant oscillation would not be modeled, such as bubble effects will lead to artificial layers in the inverted velocity depth model. Prior to the data acquisition, a far-field source signature was recorded, which only contains the source ghost (Figure 5a). This source was placed at 10 m below sea surface, and receiver was very close to the surface, so the ghost is different from the ones generated during data acquisition where the sources were at 15 m and receivers were at 22.5 m below sea surface. Before doing inversion, we estimated this source. In order to get the deghosted source signature, we simulated a synthetic source ghost according to the far-field source depth information (for 10-m depth, the corresponding time delay is 13.3 ms, and the first notch in the frequency spectrum is 75 Hz) and deconvolved it from the far-field source signature to achieve the original source without any ghost. A fourth-order Butterworth filter was applied to it with a high cut at 40 Hz (Figure 5b). Collier and Singh (1997) proposed a method to recover an appropriate source wavelet by stacking the nearest traces from several shots that acquired near sea surface over a region of relatively flat seafloor. After swell noise removal, we chose five nearest traces from five random shots from the original streamer data in the flat trench area and stacked all of them together.

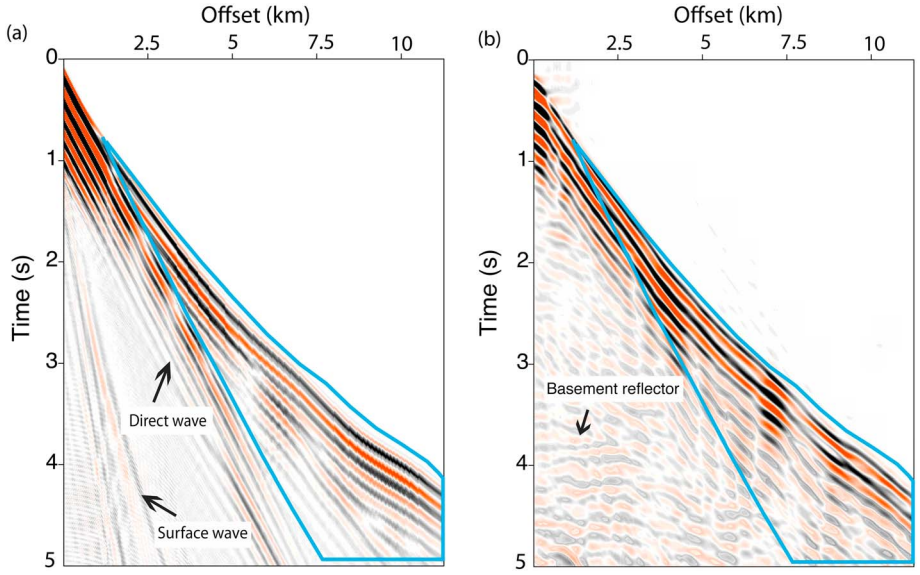

Figure 6. One of the forward modeling shot gather (a) and the observed downward continuation gather at the same shot and receiver positions (b). The blue windows show the part of data used during full waveform inversion.

We compared the wavelet obtained by stacking near offset traces with our estimated source that is incorporated with both source and receiver ghosts (source 15 m, receiver 22.5 m during the data acquisition, Figure 5c). Both of these wavelets are minimum phase reconstructed without affecting the spectral magnitude. A comparison of these two wavelets after Weiner shaping filtering is shown in Figure 5d. They fit well; the high correlation indicates that we only need to adjust the amplitude of the synthetic data by multiplying a scaling factor for the FWI based on a linearity assumption.

6.2. Inversion Strategy

The FWI of real data requires high quality of data with high signal to noise ratio. The DC has allowed to reduce the scattering effects and has brought the refraction as the first arrival. The FWI of DC data also allows us to invert wide-angle reflection data from deep structure, which was omitted during the tomographic inversion. We have a good starting velocity from the tomographic inversion of the first arrivals. To overcome the cycle skipping during FWI, we use frequencies and offsets hierarchical approach (Bunks et al., 1995; Shipp & Singh, 2002), where lower frequencies and larger offsets are inverted first, then higher frequencies and near offset data. We first invert the wide angles (both reflection and refractions) of the DC data using frequency continuation strategy and then apply the inversion to deep reflections of the original streamer data, with refining the results by gradually adding constraints from large scale to small scale. Because our streamer data are dominated by *PP* arrivals, we do not expect *S* wave velocity would be well constrained without any precondition, so we only discuss *P* wave results in the following sections. However, we do include the *S* waves in modeling. The starting S wave velocity model is built by empirical relationship (Castagna et al., 1985; Fliedner et al., 1998).

6.2.1. DC Data Inversion

As mentioned above, since the sources and receivers are near the solid seafloor, the wave theory predicts the existence of strong surface waves in the modeled data, but there are no surface waves in the DC data. In order to reduce the strong surface waves in the synthetic data, we downward extrapolated the surface streamer data to a curved surface at 75 m above the smoothed seafloor. Furthermore, there are no direct waves in the DC gathers because we mute it before performing DC, while the synthetic data include the direct wave (Figure 6a). Therefore, we only used a part of the data that contain only wide-angle arrivals (Figure 6). Similar to the tomography, we used the offset range < 11.25 km. Since the DC process does not affect the ghosts, the source and receiver ghosts are the same as that in the original streamer data; hence, we incorporated these ghosts in source wavelet before including it in forward modeling. In order to avoid creating fictitious free

surface multiples, we used an absorbing surface condition above the source and receiver locations, as we do not invert the multiple arrivals.

The whole model is 62 km long and 11 km deep. We discretized the model into 25-m grids and also removed the topmost 2-km water layer, leading to a grid size of 2,481 × 361. The time sampling interval was set to be 2 ms to keep the forward modeling stable. To avoid the dispersion, we can model frequency up to 12 Hz. Considering the arrivals of multiples and the depth of interest, we windowed the record length to 5 s. To be consistent with grid spacing, we decimated the data from 12.5-m receiver spacing to a spacing of 25 m and kept the shot interval to 100 m. A total of 439 shots and 450 receivers in each shot were used. The data were preprocessed with the standard correction (e.g., Pica et al., 1990) by multiplying the amplitudes of the real data by $\sqrt{t}$ (two-way traveltime) and convolving with $1/\sqrt{t}$ to approximately account for the 3-D to 2-D geometrical spreading. Amplitude balance has been done through source scaling factor that has been obtained by comparing the reflector of seafloor at near offset in the synthetic and real data (Igel et al., 1996; Korenaga et al., 1997). The wavefield of each shot gather was spatially resampled on the finite difference grid in such a way that the location of each shot corresponds to the closest grid node.

FWI targeted the energy related to *P* wave refraction and wide-angle reflections present in the DC gathers (Figure 6). We performed inversion from low frequency to high frequency in three main steps: 2–5, 2–9, and 2–12 Hz. The source wavelet after adding source and receiver ghosts was also filtered into the same frequency band by using the same band pass filters as the DC data. Increasing frequency components were sequentially inverted; that is, the model obtained from each frequency band was used as a starting model for next inversion step. This approach helps to minimize the risk from converging to a local minimum. For each step, 20 iterations were performed.

We started inverting all the offset simultaneously. However, after the full offset inversion, some phase and amplitude differences were still present between the observed and synthetic data at different offset ranges. Therefore, at each step, we included different offsets strategy (Shipp & Singh, 2002), starting from full offset range and then using the residual to concentrate on a particular offset range to further decrease the misfit. The data residuals were checked across the whole model during the inversion to ensure the predicted data get closer to the observed data. After 20 iterations in different frequency bands, the normalized least squares misfit reduced by 65%, 55%, and 28%, respectively (Figure S8). The misfit decreased initially rapidly and then plateaued after 10 iterations, suggesting that 20 iterations were sufficient to stop the inversion. The final inverted velocity models for each frequency band and the velocity anomaly profiles are shown in Figures 7 and S9. Since FWI used more information of the wavefield that also includes wide-angle reflection than first arrivals used in traveltime tomography, the updates cover larger areas (Figure 7). Figures 8 and S10 show the data residuals before and after the inversions of different frequency bands. For shot 200 in the first step, most of the residual energy is concentrated at near to middle offsets $<$10 km (Figure 8). After 20 iterations of waveform fitting, most residuals at near and middle offsets have been reduced. At this stage, we defined a partial window that includes the large amount of current residual in the range of offset from 7.5 to 11 km, then carried out more iterations to get a better fit model. In order to show the robustness of the inversion results, we carried out checkerboard tests that are presented in the supporting information. These test results show a consistent resolution between tomography and FWI, increasing the resolution to 250 m down to 9 km below sea surface (Figure S11).

In the frequency band of 2–5 Hz, long and intermediate wavelength structures have been recovered (Figures 7a and S9a). The whole model has been updated down to ~4 km below the seafloor due to the presence of wide-angle reflection at far offsets, except at the boundaries of the model where there are no data coverage. The velocity update is on the scale of ±0.7 km/s from the tomographic model, suggesting that the amplitude contains a significant amount of information about the sub-surface. When the inversion moves to frequency band of 2–9 Hz, more short-wavelength features are brought into the results, and the interfaces are better focused (Figure 7b). At the same time, the long and intermediate wavelength structures are also adjusted, with the maximum update value of ~0.2–0.3 km/s from the previous step. The residuals reduced significantly along the whole offset range especially at the near offset (Figure S10a), and one can see small-scale structures developing in the shallow part of the model just below the seabed (Figure 7b). The improvement from 2–9 to 2–12 Hz is not very large, the misfit reduced only by 28% after 20 iterations (Figure S8), but still we can find some short wavelength structures that are further updated in the shallow

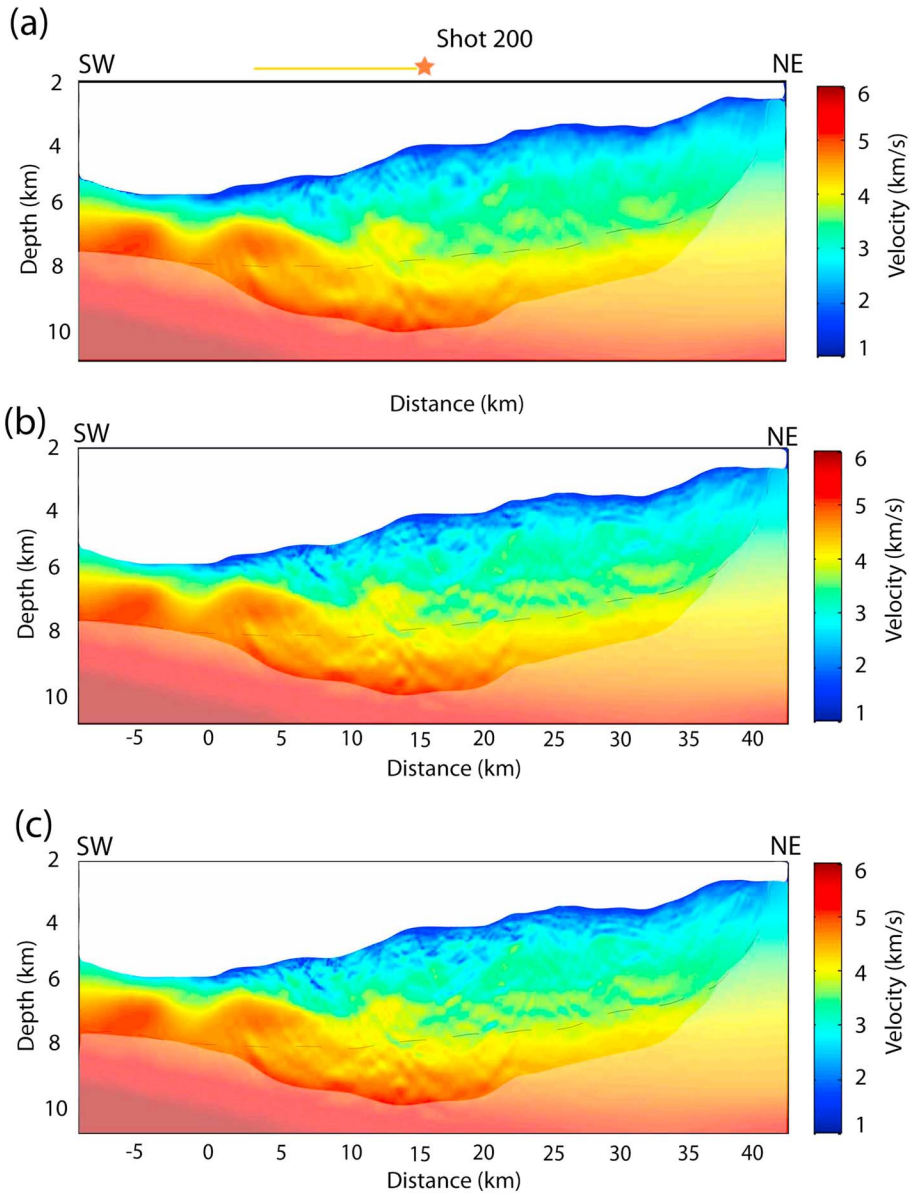

Figure 7. Full waveform inverted velocity models obtained after inverting different frequency bands: 2–5 (a), 2–9 (b), and 2–12 Hz (c). See the increase in resolution as the frequency is increased. The black dashed curve marks the ray coverage boundary of the tomography result in Figure 3b. The shadowed zone represents the area with minimal updates during the full waveform inversion.

part of the model down to ~2 km below the seafloor, especially the topmost 1 km (Figure 7c). The low-velocity structures just below the seabed have sharper boundaries than the result from the previous step, for example, in the distance range of 5 to 20 km. The final residuals are still nonzero (Figure S10b), which may due to *S* wave effects. The *S* wave velocity and attenuation parameters pose stronger effect on the waveform when the frequency is increased; however, we do not have good constraints on the *S* wave velocity. Multiparameter inversion and anisotropy or viscoelastic modeling might be needed for further improvement.

There are no turning waves in the DC data that can reach the basement at the northeast part of the model where thick sediments are present. On the other hand, the poor quality of DC data in the trench area (distance $<$0 km) do not contribute much to the FWI (Figure S5), because the near offsets contain strong

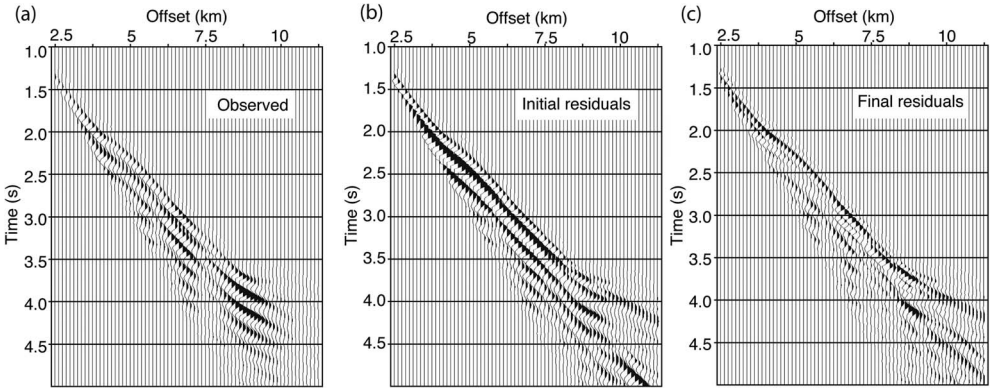

Figure 8. (a) Observed data of shot 200 (position is marked in Figure 7a) used during the 2- to 5-Hz full waveform inversion (FWI). (b) Initial residuals of shot 200 before FWI. (c) Final residuals of shot 200 after FWI.

artifacts and the signals turn weak from offset at 5 km to far offsets. To improve this result, we need to invert the original streamer data.

6.2.2. Original Streamer Data Inversion

We used the near-offset reflections in the original streamer data to further image the plate interface and the trench area, starting from the DC data waveform inverted velocity model. Apart from the band pass filter that used for swell noise removal, the preprocessing also included a subsequent deconvolution to remove spurious ringing effects (interlayer reverberation). Since the basement reflections are mixed with the first seabed multiples in some places, here we used free surface condition and deghosted source. The source wavelet was filtered as the data, and a Wiener shaping filter was used to approach the deconvolution. During this step, we only used data in 2- to 6-Hz frequency band. After 10 iterations, the model includes more detailed structures, especially the clear velocity contour ~4.5 km/s that could be used to define the continuity of the plate interface over a long distance, and the part of the model near the toe of accretionary prism contains more small-scale features (Figure 9). At the same time, the deep areas below 8-km depth have also been updated due to the usage of down going plate reflections during the inversion (Figure 9). We also computed synthetic seismograms using our final velocity model and compared them with the recorded shot gathers (Figure S12); they fit reasonably well except the 3-D diffractions. Based on theory, a FWI of turning ray data provides resolution on a scale of a wavelength; even a single frequency carries information on a broad range of wavelengths. For an average *P* wave velocity of 3 km/s and a frequency bandwidth of 2–12 Hz, the resolution will be continuously from ~250 to 1500 m, and the resolution of FWI of reflection data will be increased to a quarter of wavelength, that is, 60–70 m. Our cascaded strategy has allowed us to invert long wavelength features ($>$1.5 km) from tomography, followed by the inversion of wide-angle DC data retrieving intermediate wavelengths, and finally, short-wavelength features are retrieved using short offset reflection data. This velocity model is our final result, and we use it for the following computation and discussion.

6.3. PSDM

To further assess the improvement brought in by the FWI, we performed Kirchhoff PSDM using traveltime tomography and FWI velocities (with 100-m-scale smoothness), respectively, and compared the PSDM images. The input data were preprocessed, which included swell noise attenuation, FK filtering with antialias control, surface-related multiple elimination, high-resolution radon multiple attenuation, diffracted multiple attenuation and deconvolution in the tau-*p* domain. The sedimentary structures in the accretionary prism have been improved by using the FWI inverted result (Figure S13); however, the difference is not very significant, which indicates that the tomography result is already acceptable for the PSDM.

The final FWI velocity model and the corresponding prestack depth-migrated image are shown in Figures 10 and S14. Based on velocity anomalies (Figures S9 and 9b), the shaded parts has limited updates during the whole FWI process (Figure 10a), and the first arrivals traveltime tomography has not updated such a deep area, as well as the places beneath the topmost part of basement, though these places has been updated by the reflection FWI, the limited constraint in the starting model in the deep areas makes the velocity

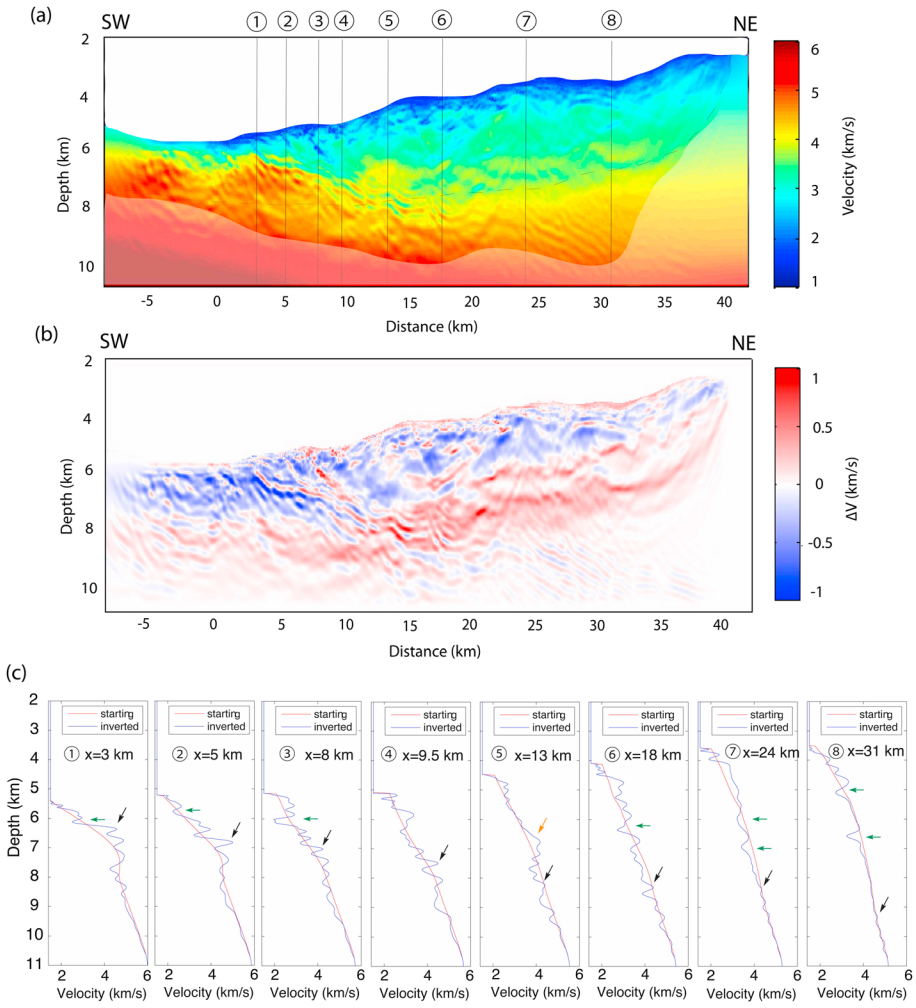

Figure 9. The final full waveform inverted velocity model obtained after the inversion of surface streamer data (a) and its corresponding velocity anomaly (b) (difference between FWI starting model and the final model). (c) Eight 1-D vertical velocity profiles extracted from the final FWI model and the starting tomography velocity model at different locations marked in (a). The red curves represent the starting model achieved by tomography, and blue curves represent the final model after the multiscale FWI. Black arrows mark the basement locations, green arrows mark the low-velocity anomaly features (dipping thrust faults in locations 1–3, backthrust in 6, and intermediate décollement in 7 and 8), and orange arrow marks the high-velocity anomaly within the forearc sediments. The black dashed curve marks the ray coverage boundary of the tomography result in Figure 3b. The shadowed zone represents the area with minimal updates during the FWI.

there is poorly constrained (Figure 10a), so we do not interpret the results in these very deep areas of the crust and the PSDM may contain uncertainties at these places.

6.4. Results

We compared our results with tomography results from the northern Sumatra (Ghosal et al., 2014; Figure S15). These two results are consistent and do not have a big difference except in the trench area, because of the existence of thick sediments in the northern Sumatra and thin sediments along profile CGGV10. We find that velocity increases to ~4.5 km/s at 6-km depth beneath the toe of the frontal slope (Figure 9), demarking the top of the subducting crust (e.g., White et al., 1992), which is consistent with the shallow basement in the time migration image (Figure S2). The basement is not smooth but shows topographic variations. Above the basement, there are several thin low-velocity layers with thickness of ~100 m sandwiched between the subducting crust and thin high-velocity layers between 5 and 15 km of distance range (Figure 10a). It is possible that these velocity oscillations could be due to the limit of the FWI model

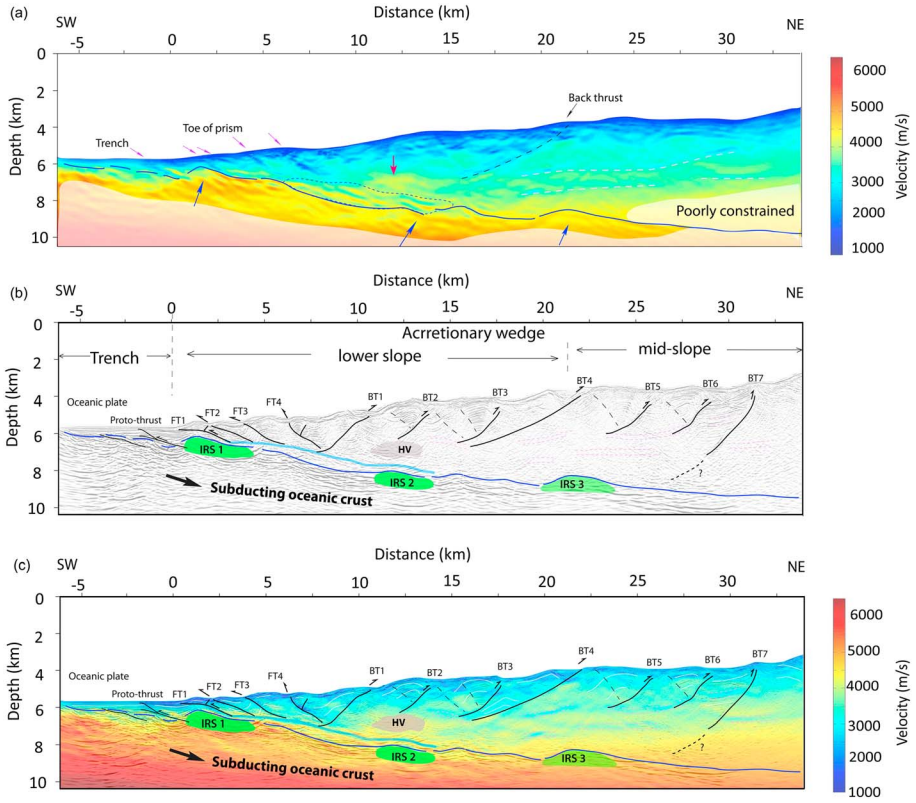

Figure 10. A combined interpretation along the frontal section of CGGV10. (a) The frontal section of the final velocity model. Blue curves indicate the top of the subducting crust; blue arrows highlight the subducting topography variations. The dashed blue curve marks a sandwich low-/high-velocity section sitting above the subducting crust. The purple arrows mark the landward dipping low-velocity structures. The black dashed line and arrow mark a seaward dipping low-velocity channel. The pink dashed lines mark the low-velocity anomalies in the middle of the wedge. The red arrow marks the high-velocity anomaly block above the subducting plate. The shadowed areas are poorly constrained by the inversion. (b) Kirchhoff prestack depth migration image with an interpretation based on the final FWI velocity model. Faults are marked by black curves; dashed black lines represent the kinks. FT: Frontal thrust, BT: Back thrust, HV: High-velocity anomaly structure marked in gray. IRS: Subducting investigator ridge segment marked in green. Blue curves indicate the plate interface. The low-velocity subduction channel above the basement is marked in light blue indicating the current position of the décollement. (c) A superposition of the velocity profile and the prestack depth migration image. The scale ratio of horizontal and vertical axis of all the panels is 1:1.

resolution at the boundary of strong velocity contrast, but their continuity suggests that they could be real. These fragmented low-velocity sections could be related to the subduction of topography high structures, which could iteratively shift the position of detachment fault due to the stress distribution changed (e.g., Lallemand et al., 1994). The sedimentary trench fill exhibits velocities from 1.8 km/s near the seafloor rapidly increasing to ~3 km/s near the basement. The velocities of the trench sediments are slightly higher than standard trench velocity near the seafloor and the topmost sediments in the accretionary prism, which could be due to the presence of sediments derived from the basaltic IR. Furthermore, as we use mainly turning rays to estimate medium to long wavelength of velocity, which is sensitive to horizontal velocity, and therefore, our estimated velocity might be slightly higher than normal velocity sediment velocity in the presence of anisotropy. The basement has high velocity of ~4.5 km/s. Immediately landward at the deformation front, the accretionary prism sediments show a gentle depth-related increase in velocity, with some landward dipping low-velocity anomalies starting from the seafloor extending down to close the basement (Figures 9 and 10a). The velocity differences between these low-velocity anomalies and the surrounding medium at the shallow (1–1.5 km) depth varies from 0.4 to 0.8 km/s at ~6 km of depth especially near 8 km of distance (1-D profiles in Figure 9). The landward dipping low-velocity features near the seafloor are likely associated with landward dipping thrust faults. There is a seaward dipping low-velocity feature at topmost 2 km of the wedge between 16 and 20 km of distance ranges,

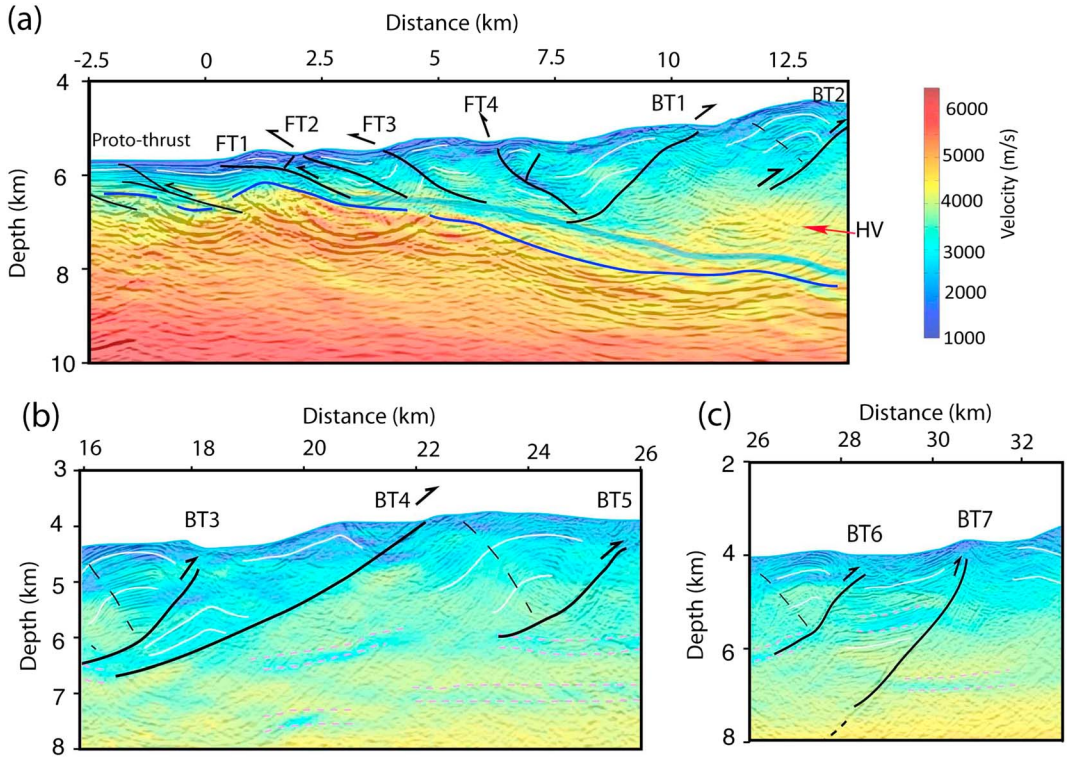

Figure 11. The blow-up sections of the superposition of velocity and PSDM results from different places along the model marked by the boxes in Figure S14a. (a) Frontal section, (b) big back thrust system BT4, and (c) deep back thrust BT7. FT: Frontal thrust marked by black curves, BT: Back thrust; HV: High-velocity anomaly structure; blue curves indicate the plate interface, and light blue indicates the current position of the décollement. The scale ratio of horizontal and vertical axes is 1:1.

which could probably be related to a backthrust (Figure 10a). There are two subhorizontal low-velocity anomalies in the middle of the wedge with a velocity anomaly of 0.5 km/s in a 300 m thick zone (see 1-D profiles at 24- and 31-km distances, Figures 9 and 10a). At the distance of 13 km, there is a high-velocity anomaly structure (~4.2 km/s) at 7-km depth, within the accretionary prism sediments (Figures 9 and 10a).

From the high-resolution PSDM image (Figure 10b), we find that the average plate dip angle beneath the trench is ~4° and beneath the accretionary prism is ~7°, but it is undulated by topographic structures, which is consistent with the inverted velocity model. The sediment thickness increases from ~1 km at the toe of the accretionary prism to ~6 km at the NE end of the profile, where the top of the subducting plate is at ~10-km depth. In the trench, a protothrust fault can be identified both in velocity model and seismic image. Toward the landward from the trench, the topmost 2- to 3-km thick accretionary prism is formed by a number of frontal thrust faults, bivergent thrust faults or kink bands that form the anticline ridges at the seabed (Figures 10 and 11). The first four frontal thrust faults (F1–F4) close to the trench cut the sedimentary sequences from the seafloor down to near the top of the oceanic crust, and they seem to be most active. Further landward, the bottom of the thrust faults seem to be connected with an intermediate low-velocity layer at ~7-km depth (Figures 10c and S16), defining the base of the bivergent fold-thrust structures. At the plate interface, there are several topographical features at the top of oceanic crust (Figure 10), and the strong lateral heterogeneities of these subducting topographic variations have caused some migration smiles at the topmost crustal reflectors, which are also related to the velocity uncertainties just beneath the topmost part of the crust.

The combined interpretation allows us to discard artifacts caused by noise and migration smiles. The most obvious feature appearing in the superimposition of the PSDM, and the velocity model is the good fitness between the shape of subducting plate and the velocity contour of ~4.5 km/s, as well as the shallow low-velocity dipping structures just below the seafloor highlighting the frontal thrust faults FT1–FT4 from the

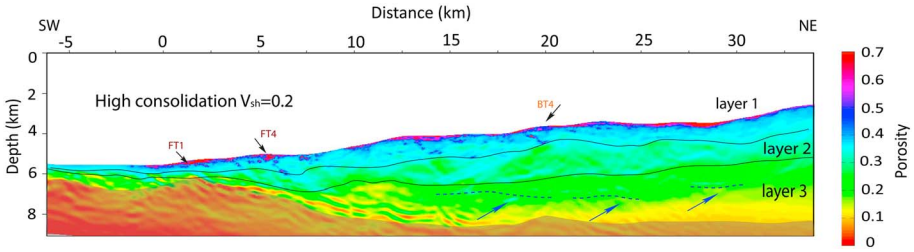

Figure 12. Porosity estimated from inverted velocity using an empirical method (Erickson & Jarrard, 1998) assuming a shale friction V_{sh} = 0.2 under high consolidation condition. The oceanic crust is shaded since the empirical method only relates to sediments.

trench to 7.5 km landward and a protothrust fault in the trench (Figures 10c and 11a). A series of seaward dipping backthrusts BT1–BT7 are distributed in the range of 10- to 32-km distance, among which BT2, BT3, BT5, and BT6 are bivergent fold-thrust structures, and BT4 associated with a low-velocity anomaly can be imaged down to ~7 km of depth in the distance range of 15–22 km (Figures 10c and 11b). The angle between the bivergent fold-thrust structures varies from 30° to 70°, and these bivergent fold-thrusts lie just above a low-velocity layer (3–3.5 km/s) in the middle of the prism at depth of ~6–7 km. This middle low-velocity layer has been considered as a pseudo-décollement leading to the formation of a backthrust (Banks & Warburton, 1986) and supported by mechanical modeling (Kuncoro et al., 2015). There are many small low-velocity anomalies in the topmost 2 km, and most of which correspond to some specific shape reflectors on the seismic reflection image (Figures 10 and 11); they may be due to some old buried low-velocity sedimentary layers, such as paleochannels, or fault-related damage zones. The high-velocity anomaly that is close to oceanic crust velocity at 7 km of depth and 12 km of distance (Figure 10) corresponds to some high-amplitude structure above the subducting plate, showing similar patterns as crustal reflections.

7. Porosity Estimation

To understand the kinematics in the accretionary wedge, it is helpful to interpret velocity in terms of fluid saturation. Therefore, in order to interpret our final inverted velocity model, we estimated the porosity from the computed velocity model. Though porosity is controlled by composition of the sediments, stress field, diagenetic effects, thermal, and many other physical parameters, constraints on porosity derived directly from those observations are lacking, and the most frequently used method is the empirical method (Erickson & Jarrard, 1998) that been tested by drilling (Hoffman & Tobin, 2004). Based on the core results of International Ocean Discovery Program (IODP) 1480 drill site in the Wharton Basin, the porosity values follow the curve with shale fraction (V_{sh}) of 0.2 under a normal consolidation condition (Erickson & Jarrard, 1998; McNeill et al., 2017). However, the accretionary prism in our study area is under high consolidation condition (Erickson & Jarrard, 1998). Assuming that the materials of the front of the wedge are from the oceanic plate, the porosity in the wedge could be not far from the curve with V_{sh} = 0.2 but under high consolidation condition. The shale fraction could also be higher, such as in Nankai (site 1173) where the shale fraction can be 0.32 (Hoffman & Tobin, 2004); therefore, we compute the porosity for both V_{sh} = 0.2 and V_{sh} = 0.4 at high consolidation situations along 40 km of well-resolved area (Figures 12 and S17) using an empirical relation given by Erickson and Jarrard (1998). Since this empirical relationship is only valid for sediments, so we do not consider the region below the plate interface. The porosities for V_{sh} = 0.2 are slightly higher than that for V_{sh} = 0.4 (Figures 12 and S17). We find that the porosity reduces laterally landward from the trench, with the lowest porosity (0–10%) at ~4-km depth beneath the seafloor at NE side of the profile. In the trench area, the low porosity is present at ~1 km below the seabed due to the presence of low porosity oceanic crust. The porosity decreases with depth, which could be due to the increase of overburden stress associated with the thickening of sedimentary layers. In the uppermost 1–1.5 km of the prism, the porosity decreases from ~70% to ~35%, suggesting the presence of unconsolidated layer (layer 1). Underneath this layer, the porosity lies between the range of 20–35%, suggesting a semiconsolidated layer 2, which also contains some high porosity layers associated with low velocities that have been interpreted as

pseudo-décollement at the base of the pop-up structures (Kuncoro et al., 2015). The differences between two estimations are not too much in layer 3; the porosity decreases slowly and approaches 0 at the bottom of sediments section (Figures 12 and S17), suggesting that below this depth the sediments are highly compacted (layer 3). These results are not too far from the IODP results in Wharton Basin, where the top-most sediments porosity reach ~80%, then it reduces to 30%–40% rapidly, and lies in the range of 10%–20% near the basement (McNeill et al., 2017). The layer at depth of ~7 km, marked by the dashed curves (Figures 12 and S17), has a porosity of ~20%–25%. The porosity of most of the landward dipping thrust faults at the toe of prism is higher than 40%, and that of the backthrust (BT1) is ~35%, suggesting high fluid saturation. We also compute the effective stress and pore pressure (see supporting information, Figure S18, Davis et al., 1983; Kitajima & Saffer, 2012; Tobin & Saffer, 2009). The estimated pore pressure we obtained could indicate in situ mechanical loading, mineral dehydration, and heterogeneous drainage along faults in the prism and along the décollement. However, as mentioned earlier, the empirical method is not 100% accurate, so the porosity values we obtained should contain some uncertainties, and hence, the effective stress values, which are based on the assumption of the fully locking status and the accretionary prism is in a critical state that under lateral compression, and therefore, these computed parameters are only an estimation.

8. Discussion

8.1. Subducting Plate

The deformation front has an irregular structure possibly due to the basement topography related to the IR. The down going plate here is characterized by variable basement topography, which also controls the variations of sediment thickness above the plate interface. The IR is ~105 km wide from the bathymetric map and is characterized by four linear ridges, and our profile crosses the easternmost one. The complex basement topography below the forearc (Figure 10) could be related to subduction of the eastern branch of this ridge. Another seismic profile CGGV11 crosses the whole IR and intersects CGGV10 at 35° (Figure S19a). This branch of ridge shows a long slope appearance since it is the eastern boundary of IR (Figure S19), and there are several reactivated basement high features in this segment; the two in the east side could be related to active normal faults (Figure S19b); the landward projections of these structures are imaged on profile CGGV10, as shown in our results. These isolated crustal highs on the subducting plate, which are marked as the IR Segments (IRS), seem to control the fold-thrust positions in the accretionary wedge; for example, IRS 1 has influenced the first fold at the toe that is bounded by bivergent thrusts, and the uplift of the middle slope boundary is located above IRS 3. There are some high-amplitude reflections near the top of the oceanic crust seaward off IRS 2 (Figure 10a; 8–13 km of distance), where the velocity has some low perturbations, which may be due to the fluid-rich sediments that have been entrained with subducting topographic high structures IRS 2 (Bell et al., 2010), and the subducting of reactivated normal faults (Figure S19) could also enhance the weak zones around IRS 2.

At the northern Sumatra margin (Dean et al., 2010; Ghosal et al., 2014) and western Java (Kopp et al., 2009), a décollement seems to form a detachment between the upper deforming accretionary prism and the underthrusting sedimentary sequence (Chapple, 1978; Davis et al., 1983). In our velocity depth profile (Figures 9, 10, and S16b), there is a ~300-m-thick low-velocity layer (3.5–4 km/s) above the top of basement in the distance range of 3–15 km. This low-velocity layer can be identified just sitting above the IRS 1, and its consistency is kept down to the top of IRS 2, which we interpret as the décollement for this region, assuming it is not due to the limitation of FWI illumination at the boundary of strong velocity contrast. It is not a perfect one layer and has been fragmented between IRS 1 and IRS 2 (Figure 10a), which could be due to the process of iteratively searching the weak path that generated by the IRS2 passing through, the upward jumping of the décollement, and it is in a good agreement with the synthetic studies that suggest the décollement follows the subducted flank of the subducting high structures and is deflected upwards (e.g., Dominguez et al., 1998; Lallemand et al., 1994).

The porosity in this décollement is ~20–25% (Figure 12), which is consistent with the result from Tsuji et al. (2008). The effective stress $\sigma_v^{'}$ along the décollement is nearly constant from 0 to 15 km distance landward from the trench, which is similar to other subduction zones such as Nankai (Tobin & Saffer, 2009). This low-velocity layer could be due to the presence of fluid-filled trench sediments that have been brought

by the downgoing plate forming a subduction channel between the plate interface (e.g., Cloos & Shreve, 1988a, 1988b), especially the entrainment carried by the subducting topographic highs. The porous sediments subducting with the incoming plate will be subjected to a progressive increase in tectonic and overburden stresses as they are accreted to the upper plate or subducted with the down going plate. The dissipation of pressure leads to rapid consolidation and dewatering, which are generally most pronounced near the trench (Saffer et al., 2000; Saffer & Tobin, 2011). Subducted sediments host bound water that become an important source of fluids when the temperatures are sufficient to drive dehydration reactions, which is dominant by the transformation of smectite to illite clay over a temperature range of ~60–150 °C (Bekins & Dreiss, 1994; Moore & Vrolijk, 1992; Vrolijk et al., 1991). The previous study of the heat flow and the drilling data near our study area (Heat Flow Data, n.d.) indicate that the temperature is ~170 °C at ~3 km below the seafloor near the IR in the oceanic basin. Though the temperature would be lower at the subducting plate interface at the same depth (e.g., Hippchen & Hyndam, 2008), it still would lie in the temperature range of smectite dehydration. Furthermore, high heat flows have been found offshore central Sumatra (Hendrawan & Draniswari, 2016; Heat Flow Data, n.d.), which means the margin in our study area is warm; hence, the illitization could start at $<$10 km distance from the trench and illitization source is in the range of ~8–28 km from the trench (Lauer & Saffer, 2015). The end of the subduction channel in our result is at ~15 km of distance from the trench and covered by 3- to 3.5-km-thick accretionary sediments (Figure 10), where the temperatures are high enough for the smectite dehydration. From the 1-D velocity profiles (Figure 9), the velocities drop of ~0.5–0.8 km/s above the basement at locations 4–6 suggests that the fluid content could reach 20–30% and is consistent with our porosity profile. The illitization could strengthen the medium during the dewatering process and increase the velocity of medium to be as high as quartz ($>$5 km/s) (Tudge & Tobin, 2013). The thermal fluid in the subduction channel could enhance the illitization process and generate a hard cap at the top of this weak layer to trap the overpressured fluid, as some thin high-velocity segments that are located above and around the décollement in our results (Figure 10).

On the other hand, the subduction erosion of lithified rocks from the upper plate could also provide the excess materials for the subduction channel (Cloos & Shreve, 1988a, 1988b). The topographic highs of the down going plate could have been cut off within the subduction channel shear zone by the highly compacted upper plate at a certain depth once the pressure is high enough (Cloos & Shreve, 1996). The large basaltic detached bodies from the lower plate, such as the high-velocity body HV (Figure 10), could get underplated in the upper plate. The sediment-filled subduction channel is thin in our imaging domain, and the top of subducting topographic highs jammed against the base of overriding block could act as a stick-slip seismic asperity (Cloos, 1992; Cloos & Shreve, 1996), possibly producing large earthquakes, such as the Padang 1797 event.

8.2. Upper Plate (Accretionary Prism)

The fontal prism is formed by adding of the trench sediments to the toe of active convergent margins and slumped debris from upper plate (Von Huene et al., 2004). The subduction stress causes the pressure within the accreted sequence to deform at the deformation front and pushed landward (e.g., Tsuji et al., 2008). Our results show that the uppermost sedimentary section of the accretionary prism has low velocity and high porosity, suggesting that these sediments remain uncompacted and unlithified for over 30–40 km landward off the trench. These low velocities are mainly associated with frontal thrust faults and bivergent folds. The protothrust fault and four major frontal thrust faults (F1–F4) coincide with the low-velocity landward dipping structures (Figure 10), indicating that these faults are probably active and act as highly effective conduits for the dewatering along the décollement. The back thrust faults that bound the bivergent fault-bend folds (BT1, BT2, BT3, BT5, and BT6) between 10 and 30 km of distance range and a high dipping angle backthrust BT7 do not display obvious low-velocity anomaly features, suggesting low water saturation along them. However, these faults are potentially important conduits for fluid flow generated by illitization within the prism and manifest the inception of faulting at the deformation front. A large seaward dipping (landward vergent) low-velocity channel is associated with the backthrust BT4, which has also been suggested by mechanical modeling (Kuncoro et al., 2015). BT7 penetrates much deeper down to the poorly imaged zone and shows landward vergent; the sediments further NE side off BT7 show seaward vergent, suggesting that BT7 could be close to the transition zone of two vergent sediments.

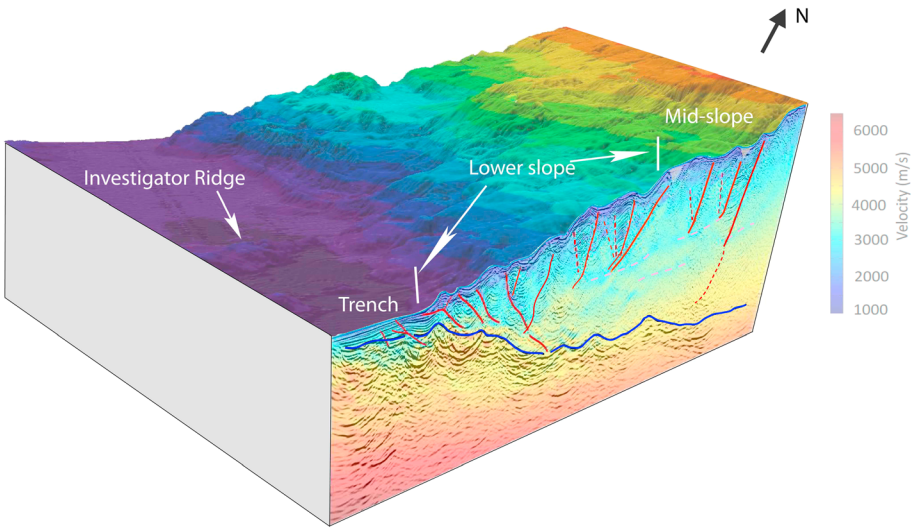

Figure 13. A 3-D perspective view by combining the pre-stack depth migrated seismic image with the FWI velocity profile, and the high-resolution bathymetric map.

Usually, the subduction process prefers to generate folding in the trench deposits and seaward vergent thrust faulting (Byrne et al., 1988; MacKay et al., 1992); the presence of landward vergent thrusts is relatively uncommon in the previous publications, but it has also been found along the Sumatra subduction zone (McNeill & Henstock, 2014; Moeremans et al., 2014) and just north off our study area (Cook et al., 2014). Along our profile, the faults show both vergents, probably because the compressional stress induced by subducting topographic high structures, especially the sliced basaltic segment (HV), which may contribute to the change of vergent. These observations indicate the locking status of the shallow megathrust that lead to high lateral compressive stress.

The low-velocity anomaly structures in the shallow part of accretionary prism probably related to dewatering process, gravity-related deformation, fault-related cementation and mineralization (e.g., Chan et al., 2000; Knipe, 1992), or decrease of rigidity in the upper sediments through loss of initial cementation. For temperatures $<$60 °C, the interlayer water release is only due to a simple compaction controlled by mechanical and the physical properties (Colten-Bradley, 1987). The lateral compression associated with the subduction process further landward has led to the increase of velocity possibly due to compaction-associated fluid expulsion. The overall velocity increases while porosity decreases with increasing depth, which means that the compaction and lithification effects increase with depth. The cause of these porosity and velocity changes may result from lithological heterogeneity. The velocity of smectite could vary from 1.5 to 5 km/s, depending on porosity (Tudge & Tobin, 2013). In our case the high-velocity structures in layer 2 could be illite-rich sediments (Figure 12), for example, the high-velocity anomaly structures at the topmost 2 km where the *P* wave velocity is ~3.5 km/s (1-D section 4 in Figure 9 at depth of ~6 km). On the other hand, the fault-related chemical alteration and mechanical damage also produce weak zones along fault damage zones, which is facilitated by fault-controlled fluid flow that controls further accommodation of mechanical deformation. By using the distribution of fault-related calcite cement as an indicator of paleofluid migration, fault-parallel fluid flow can get focused along fault segments (e.g., Kristensen et al., 2016). The inverted velocity results show that the damage zone could be hundred meters scale (~200–300 m), which combined with porosity values could be useful for predicting the fluid properties.

Previous studies show that the accretionary wedge offshore the central Sumatra can be divided into three strike-parallel belts: the frontal prism, midslope break, and terrace (Cook et al., 2014). In our result, from the top of the BT4 (at ~20 km, Figure 10) to further NE, the topography changes on a larger scale than within the accretionary prism toe. The 3-D view of our study area shows that the outermost slope is variable (Figure 13). BT4 might act as a separator between the SW lower slope that is steep and rugged, and the midslope of the accretionary wedge is characterized by a relatively smooth topography. The structures in

our profile do not show a good continuity toward the north following the bathymetric morphology, which is because of the subducting of IR. The very complex structures of IR make the subduction process damage the original topography of the accretionary prism, generating very varied bathymetric features (Figure 13). Our seismic velocity profile fits well with the local bathymetric structures, and the frontal thrust faults seem to be active, indicating that our study area is almost at the NW end of the Mentawai locked zone.

8.3. Psudo-Décollement

We observed a discontinuous low-velocity anomaly layer ~3 km below the seafloor within the accretionary sediments starting from 15 km landward, near the high-velocity body HV (Figures 10 and S16a). The velocity of this layer is ~0.5 km/s lower than the surrounding areas. This area is still in the range of peak illitization source (10–28 km landward from the trench; Lauer & Saffer, 2015). The increase of sediment thickness along the subduction causes increasing vertical stress during burial and lateral compression due to tectonic stress, and this tectonic squeeze leads to water loss. When the temperature reaches in the range of $>$60 °C, the effects of mechanical compaction become less important and temperature-controlled chemical changes become dominant. Then the transformation of the weak smectite to stiff illite clay makes the indurated sediment to form strong accretionary prism by fluids release in the deeper sediment section (e.g., Moore & Vrolijk, 1992). At the same time, if this is a boundary between different lithological compositions, diagenetic reactions may also have expelled fluid, or migration of fluid into this interval (e.g., IODP, Hüpers et al., 2017). This intermediate low-velocity channel shows overpressured, low effective stress (Figure S18), suggesting it is mechanically weak. Therefore, it could provide a low basal shear stress and develop landward vergent structures. On the other hand, the high porosity may indicate the fluid migration along this layer, which could help different mineral precipitations healing this weak layer and making it difficult to be imaged on the seismic profile.

This weak layer in the middle of accretionary prism is interpreted as a pseudo-décollement (Kuncoro et al., 2015), and here we observed it as a low-velocity zone; hence, it is a real physical layer. This layer could be formed by subhorizontal branches of different thrust faults (Ramps) that rise from the subducting plate boundary, or some connected duplex structures. However, its limited length of our study area and the poor imaging of deeper structures could not provide a certain answer. Low-velocity layers just above the basement and in the middle of the incoming sediments have been imaged in the oceanic basin off north Sumatra (Qin & Singh, 2017), which could act as primary or secondary décollement and act as a conveyer belt for bivergent fault-bend folds above to move landward. The formation of multisub layers of this middle wedge weak zone may be due to the erosion and subsequent migration of subsiding older forearc sediments.

Similar to the Nankai Trough subduction zone (Tsuji et al., 2014), the accretionary prism in our study area has been separated by the pseudo-décollement into two layers, where the top 2–3 km is a high reflectivity zone of the incoming plate sediments that are offscraped and frontally accreted. Below this layer down to the subducting plate lies a low reflectivity sedimentary zone, which is formed by older forearc sediments. The velocity increases with depth in this old sedimentary section, from ~4 km/s at the bottom of the pseudo-décollement linearly increases to the crustal velocity (Figure 9c), which indicates that the sediments are highly compacted and lithified. However, our velocity result has poor constraints in this region due to limited offset of 15 km; longer offset data are required to further constrain this layer.

8.4. Tsunami Potential

There is a strong link between the rupture propagation reaching to the trench and tsunami generation (e.g., Gulick et al., 2011; Ide et al., 2011; Kodaira et al., 2012; Ozawa et al., 2011; Wei et al., 2012). The last great earthquake that ruptured this Mentawai segment occurred in 1833, and since then a slip of ~10 m has been accumulated assuming a plate convergence rate of 55 mm/year. As mentioned earlier, our observations indicate that this frontal section is locked, and if we assume it is full coupling, the accumulated stress may lead to progressive consolidation and lithification. The asperities on the subducting plate due to the IR could serve to limit rupture propagation during some earthquakes but could eventually rupture during other events with large slip, as was the case for the 2011 Tohoku earthquake (Simons et al., 2011). The shallow décollement may act as a focus for plate boundary slip as a seismogenic décollement

(Dean et al., 2010; Hubbard et al., 2015; Moore & Saffer, 2001; Tsuji et al., 2008). Dynamic weakening of faults at high slip rate by melt lubrication and fluidization during an earthquake could be possible factors controlling coseismic deformation mechanisms and causing the large slip near the trench (Romano et al., 2014; Ujiie & Kimura, 2014). A huge shallow slip occurred during the 2011 Tohoku earthquake along the Japan Trench that was attributed to the abundance weak, smectite-rich fault zone and thermal pressurization effects, which can facilitate fault slip during the earthquake (Fulton et al., 2013; Ujiie et al., 2013). The existence of low-velocity faults in our results with rich water content and low friction is similar to the case of Japan Trench. On the contrary, in the north Sumatra, where the sedimentary layer is much thicker (4–5 km) than Mentawai area, the diagenesis strength of clay-rich faults before subduction may drive shallow slip and may have increased the 2004 *Mw* = 9.2 Sumatra-Andaman earthquake rupture width and magnitude (Hüpers et al., 2017).

Besides sediment effects, coseismic splay faulting is often invoked for seafloor uplift. Slip on preexisting splay faults off the plate interface is also a viable mechanism for large tsunamigenesis (e.g., Fukao, 1979; Moore et al., 2007). The coseismic slip distribution of the 1944 Tonankai earthquake (*Mw* = 8.1) based on tsunami and seismic waveform inversions suggests that the earthquake rupture propagated along a megasplay fault that branches from the plate boundary megathrust and cuts through the prism (Kikuchi et al., 2003; Tanioka & Satake, 2001). The preexisting weak frontal thrusts at the toe of the prism in our results should provide a path for rupturing the updip portion of the subduction thrust interface with low rupture velocities. Also, high pore pressures along these structures could be linked to slow rupture propagation and large seafloor uplift (Sugioka et al., 2012).

The topmost of the wedge in our result is highly water saturated, and the effective stress is low. Once the pore pressure reaches at a certain point, hydrofractures at supralithostatic fluid pressures may occur. If the magnitude of the earthquake is big enough, the subsequent shaking can make water-saturated sediment temporarily lose strength and act as a fluid and may lead to landslide, which is another mechanism for tsunami generation. Such as a previous study of 2011 Tohoku earthquake suggest that a submarine landslide might have occurred near the trench (Grilli et al., 2013).

9. Conclusions

Fault interpretations from seismic data are commonly represented as thin lines on a seismic cross section and treat faults as simple two-dimensional surfaces, whereas they in reality are three-dimensional zones containing a range of subseismic structures. By applying combination of DC, traveltime tomography, and multiscale FWI to ultralong offset seismic streamer data from the frontal section of the northern Mentawai locked zone, a well-constrained velocity model has been retrieved, which is consistent with PSDM seismic result. These two results give us an idea of the range of fault-related damage zone, which are useful for the understanding the formation and evolution of these faults. According to our quantitative subsurface profiles, the following conclusions can be made:

1. The plate interface has been well imaged along our profile at the subduction front, including several subducting topographic high structures and a piece of detached basaltic crust in the accretionary sediments.
2. A low-velocity décollement is imaged containing fluids sitting above the down going basement, connecting several frontal thrust faults that are likely active at the toe of accretionary prism.
3. An overpressured pseudo-décollement has been found in the accretionary prism that connects with the roots of bivergent structures in the top part of the wedge, separating the prism into upper and lower two segments with strong and weak reflections, respectively.

The variable topography of downgoing plate relates to the east branch of IR and contributes to generating the sliced basaltic body in the wedge. This locked frontal section of Mentawai could rupture during an earthquake and produce tsunamis. Furthermore, the pseudo-décollement separating the old and young sediments in the wedge connects the roots of bivergent folds and acts as a conveyer belt in preserving these structures in the forearc region. It could also play a key role in the rupture propagation, controlling the updip limit of the seismogenic zone and influencing the coseismic rupture propagation during an earthquake.

Acknowledgments
We thank CGGV for providing the data. We also thank Nugroho D. Hananto for his contribution to the data acquisition. Discussions with Lidia Lonergan and Kyle Edward Bradley are very helpful to improve the interpretation. Numerical computations were partly performed on the S-CAPAD platform, IPGP, France. This work was partly performed using HPC resources from GENCI-[TGCC/CINES/IDRIS] (Grant 2014-[100376]). This is IPGP contribution 3983. This is EOS contribution 219.

References

Aki, K. (1979). Characterization of barriers on an earthquake fault. *Journal of Geophysical Research*, *84*(B11), 6140–6148. https://doi.org/10.1029/JB084iB11p06140

Ammon, C. J., Ji, C., Thio, H. K., Robinson, D., Ni, S., Hjorleifsdottir, V., et al. (2005). Rupture process of the 2004 Sumatra-Andaman earthquake. *Science*, *308*(5725), 1133–1139. https://doi.org/10.1126/science.1112260

Arnulf, A., Harding, A. J., Singh, S. C., Kent, G. M., & Crawford, W. (2011). Strong seismic heterogeneity in layer 2A near hydrothermal vents at the mid-Atlantic ridge. *Geophysical Research Letters*, *38*, L13320. https://doi.org/10.1029/2011GL047753

Arnulf, A., Harding, A. J., Singh, S. C., Kent, G. M., & Crawford, W. (2014). Nature of upper crust beneath the lucky strike volcano using elastic full waveform inversion of streamer data. *Geophysical Journal International*, *196*(3), 1471–1491. https://doi.org/10.1093/gji/ggt461

Bangs, N. L. B., Westbrook, G. K., Ladd, J. W., & Buhl, P. (1990). Seismic velocities from the Barbados Ridge complex: Indicators of high pore fluid pressures in an accretionary Complex. *Journal of Geophysical Research*, *95*, 8767–8782. https://doi.org/10.1029/JB095iB06p08767

Banks, C. J., & Warburton, J. (1986). "Passive-roof" duplex geometry in the frontal structure of the Kirthar and Sulaiman mountain belts, Pakistan. *Journal of Structural Geology*, *8*(3-4), 229–237. https://doi.org/10.1016/0191-8141(86)90045-3

Bekins, B. A., & Dreiss, S. J. (1994). Influence of kinetics on the smectite to illite transition in the Barbados accretionary prism. *Journal of Geophysical Research*, *99*(B9), 18,147–18,158. https://doi.org/10.1029/94JB01187

Bell, R., Sutherland, R., Barker, D. H. N., Henrys, S., Bannister, S., Wallace, L., & Beavan, J. (2010). Seismic reflection character of the Hikurangi subduction interface, New Zealand, in the region of repeated Gisborne slow slip events. *Geophysical Journal International*, *180*(1), 34–48. https://doi.org/10.1111/j.1365-246X.2009.04401.x

Berryhill, J. R. (1979). Wave equation datuming. *Geophysics*, *44*(8), 1329–1344. https://doi.org/10.1190/1.1441010

Berryhill, J. R. (1984). Wave-equation datuming before stack. *Geophysics*, *49*(11), 2064–2066. https://doi.org/10.1190/1.1441620

Bilek, S. L., Schwartz, S. Y., & DeShon, H. R. (2003). Control of seafloor roughness on earthquake rupture behavior. *Geology*, *31*(5), 455–458. https://doi.org/10.1130/0091-7613(2003)031<0455:COSROE>2.0.CO;2

Briggs, R. W., Sieh, K., Meltzner, A., Natawidjaja, D., Galetzka, J., Suwargadi, B., et al. (2006). Deformation and slip along the Sunda megathrust in the great 2005 Nias-Simelue earthquake. *Science*, *311*(5769), 1897–1901. https://doi.org/10.1126/science.1122602

Bunks, C., Saleck, F. M., Zaleski, S., & Chavent, G. (1995). Multiscale seismic waveform inversion. *Geophysics*, *60*(5), 1457–1473. https://doi.org/10.1190/1.1443880

Byrne, D. E., Davis, D. M., & Sykes, L. R. (1988). Loci and maximum size of thrust earthquakes and the mechanics of the shallow region of subduction zones. *Tectonics*, *7*(4), 833–857. https://doi.org/10.1029/TC007i004p00833

Calahorrano, B. A., Sallarès, V., Collot, J. Y., Sage, F., & Ranero, C. R. (2008). Nonlinear variations of the physical properties along the southern Ecuador subduction channel: Results from depth-migrated seismic data. *Earth and Planetary Science Letters*, *267*(3-4), 453–467. https://doi.org/10.1016/j.epsl.2007.11.061

Castagna, J. P., Batzle, M. L., & Eastwood, R. L. (1985). Relationships between compressional-wave and shear-wave velocities in elastic silicate rocks. *Geophysics*, *50*(4), 571–581. https://doi.org/10.1190/1.1441933

Chan, M. A., Parry, W., & Bowman, J. (2000). Diagenetic hematite and manganese oxides and fault-related fluid flow in Jurassic sandstones, Southeastern Utah. *AAPG Bulletin*, *84*, 1281–1310.

Chapple, W. M. (1978). Mechanics of thin-skinned fold-and-thrust belts. *Geological Society of America Bulletin*, *89*(8), 1189–1198. https://doi.org/10.1130/0016-7606(1978)89<1189:MOTFB>2.0.CO;2

Chlieh, M., Avouac, J. P., Sieh, K., Natawidjaja, D. H., & Galetzka, J. (2008). Heterogeneous coupling of the Sumatran megathrust constrained by geodetic and paleogeodetic measurements. *Journal of Geophysical Research*, *113*, B05305. https://doi.org/10.1029/2007JB004981

Cloos, M. (1992). Thrust-type subduction-zone earthquakes and seamount asperities: A physical model for seismic rupture. *Geology*, *20*(7), 601–604. https://doi.org/10.1130/0091-7613(1992)020<0601:TTSZEA>2.3.CO;2

Cloos, M., & Shreve, R. L. (1988a). Subduction channel model of prism accretion, melange formation, sediment subduction, and subduction erosion at convergent plate margins: 1. Background and description. *Pure and Applied Geophysics*, *128*, 455–500.

Cloos, M., & Shreve, R. L. (1988b). Subduction channel model of prism accretion, mélange formation, sediment subduction, and subduction erosion at convergent plate margins: 2. Implications and discussion. *Pure and Applied Geophysics*, *128*(3-4), 501–545. https://doi.org/10.1007/BF00874549

Cloos, M., & Shreve, R. L. (1996). Shear-zone thickness and the seismicity of Chilean- and Marianas-type subduction zones. *Geology*, *24*(2), 107–110. https://doi.org/10.1130/0091-7613(1996)024<0107:SZTATS>2.3.CO;2

Collier, J. S., & Singh, S. C. (1997). Detailed structure of the top of the melt body beneath the East Pacific rise at 9°40′N from waveform inversion of seismic reflection data. *Journal of Geophysical Research*, *1022*, 20,287–20,304. https://doi.org/10.1029/97JB01514

Colten-Bradley, V. A. (1987). Role of pressure in smectite dehydration-effects on geopressure and smectite-to-illite transformation. *American Association of Petroleum Geologists Bulletin*, *71*, 1414–1427.

Cook, B. J., Henstock, T. J., McNeill, L. C., & Bull, J. M. (2014). Controls on spatial and temporal evolution of prism faulting and relationships to plate boundary slip offshore north-Central Sumatra. *Journal of Geophysical Research: Solid Earth*, *119*, 5594–5612. https://doi.org/10.1002/2013JB010834

Davis, D. M., Suppe, J., & Dahlen, F. A. (1983). Mechanics of fold-and-thrust belts and accretionary wedges. *Journal of Geophysical Research*, *88*(B2), 1153–1172. https://doi.org/10.1029/JB088iB02p01153

Dean, S. M., McNeill, L. C., Henstock, T. J., Bull, J. M., Gulick, S. P. S., Austin, J. A., et al. (2010). Contrasting Décollement and prism properties over the Sumatra 2004-2005 earthquake rupture boundary. *Science*, *329*(5988), 207–210. https://doi.org/10.1126/science.1189373

Dominguez, S., Lallemand, S., Malavieille, J., & Schnuerle, P. (1998). Oblique subduction of the Gagua ridge beneath the Ryukyu accretionary wedge system: Insights from marine observations and sandbox experiments. *Marine Geophysical Researches*, *20*(5), 383–402. https://doi.org/10.1023/A:1004614506345

Dominguez, S., Malavielle, J., & Lallemand, S. E. (2000). Deformation on accretionary wedges in response to seamount subduction: Insights form sandbox experiments. *Tectonics*, *19*(1), 182–196. https://doi.org/10.1029/1999TC900055

Erickson, S., & Jarrard, R. (1998). Velocity-porosity relationships for water-saturated siliciclastic sediments. *Journal of Geophysical Research*, *103*(B12), 30,385–30,406. https://doi.org/10.1029/98JB02128

Feng, L., Hill, E. M., Banerjee, P., Hermawan, I., Tsang, L. L. H., Natawidjaja, D. H., et al. (2015). A unified GPS-based earthquake catalog for the Sumatran plate boundary between 2002 and 2013. *Journal of Geophysical Research: Solid Earth*, *120*, 3566–3598. https://doi.org/10.1002/2014JB011661

Fliedner, M. M, White, R. S., & Smallwood, J. R. (1998). Seismic velocity structure of basalt flows. SEG Expanded Abstracts, SP4.5, 1178–1181.

Fukao, Y. (1979). Tsunami earthquakes and subduction processes near deep-sea trenches. *Journal of Geophysical Research*, *84*(B5), 2303–2314. https://doi.org/10.1029/JB084iB05p02303

Fuller, C. W., Willett, S. D., & Brandon, M. T. (2006). Formation of forearc basins and their influence on subduction zone earthquakes. *Geology*, *34*(2), 65–68. https://doi.org/10.1130/G21828.1

Fulton, P. M., Brodsky, E. E., Kano, Y., Mori, J., Chester, F., Ishikawa, T., et al. (2013). Low Coseismic friction on the Tohoku-oki fault determined from temperature measurements. *Science*, *342*(6163), 1214–1217. https://doi.org/10.1126/science.1243641

Gahalaut, V. K., Nagarajan, B., Catherine, J. K., & Kumar, S. (2006). Constraints 2004 Sumatra-Andaman earthquake rupture from GPS measurements in Andaman-Nicobar Islands. *Earth and Planetary Science Letters*, *242*(3), 365–374.

Gardner, G. H. F., Gardner, L. W., & Gregory, A. R. (1974). Formation velocity and density: The diagnostic basics for stratigraphic traps. *Geophysics*, *39*, 770–780.

Geist, E. L., Bilek, S. L., Arcas, D., & Titov, V. V. (2006). Differences in tsunami generation between the December 26, 2004 and March 28, 2005 Sumatra earthquakes. *Earth, Planets and Space*, *58*, 185–193.

Ghosal, D., Singh, S. C., & Martin, J. (2014). Shallow subsurface morphotectonics of the NW Sumatra subduction system using an integrated seismic imaging technique. *Geophysical Journal International*, *198*, 1818–1831.

Grilli, S. T., Harris, J. C., Tajalli Bakhsh, T. S., Masterlark, T. L., Kyriakopoulos, C., Kirby, J. T., & Shi, F. (2013). Numerical simulation of the 2011 Tohoku tsunami based on a new transient FEM co-seismic source: Comparison to far- and near-field observations. *Pure and Applied Geophysics*, *170*(6-8), 1333–1359.

Gulick, S. P. S., Austin, J. A., McNeill, L. C., Bangs, N. L. B., Martin, K. M., Henstock, T. J., et al. (2011). Updip rupture of the 2004 Sumatra earthquake extended by thick indurated sediments. *Nature Geoscience*, *4*(7), 453–456. https://doi.org/10.1038/ngeo1176

Hamilton, E. L. (1978). Sound velocity-density relations in sea-floor sediments and rocks. *Acoustical Society of America Journal*, *63*, 366–377.

Hearn, T. M., & Ni, J. F. (1994). Pn velocities beneath continental collision zones: The Trukish-Iranian Plateau. *Geophysical Journal International*, *117*, 273–283.

Heat Flow Data (n.d.) Royal Holloway South East Asia research group (http://searg.rhul.ac.uk/current-research/heat-flow/).

Hendrawan, R. N., & Draniswari, W. A. (2016). Assessing the possibility of Enhanced Geothermal System in western Indonesia. *Earth and Environmental Science*. https://doi.org/10.1088/1755-1315/42/1/012021

Henig, A. S., Blackman, D. K., Harding, A. J., Canales, J. -P., & Kent, G. M. (2012). Downward continued multichannel seismic refraction analysis of Atlantis Massif oceanic core complex, 30°N, Mid-Atlantic Ridge. *Geochemistry, Geophysics, Geosystems*, *13*, Q0AG07. https://doi.org/10.1029/2012GC004059

Hill, E. M., Borrero, J. C., Huang, Z., Qiu, Q., Banerjee, P., Natawidjaja, D. H., et al. (2012). The 2010 Mw 7.8 Mentawai Earthquake determined from tsunami field survey and near-field GPS data. *Journal of Geophysical Research*, *117*, B06402. https://doi.org/10.1029/2012JB009159

Hippchen, S., & Hyndam, R. D. (2008). Thermal and structural models of the Sumatra subduction zone: Implications for the megathrust seismogenic zone. *Journal of Geophysical Research*, *113*, B12103. https://doi.org/10.1029/2008JB005698

Hoffman, N. W., & Tobin, H. J. (2004). An empirical relationship between velocity and porosity for underthrust sediments in the Nankai Trough accretionary prism. In H. Mikada, G. F. Moore, A. Taira, K. Becker, J. C. Moore, & A. Klaus (Eds.), *Proceedings of the Ocean Drilling Program, Sci. Results*, (Vol. 190-196, pp. 1–23).

Hubbard, J., Barbot, S., Hill, E. M., & Tapponnier, P. (2015). Coseismic slip on shallow décollement megathrusts: Implications for seismic and tsunami hazard. *Earth-Science Reviews*, *141*, 45–55.

Hüpers, A., Torres, M. E., Owari, S., McNeill, L. C., Dugan, B., Henstock, T. J., et al. (2017). Release of mineral-bound water prior to subduction tied to shallow seismogenic slip off Sumatra. *Science*, *356*(6340), 841–844. https://doi.org/10.1126/science.aal3429

Husen, S., Kissling, E., & Quintero, R. (2002). Tomographic evidence for a subducted seamount beneath the Gulf of Nicoya, Costa Rica: The cause of the 1990 Mw = 7.0 Gulf of Nicoya earthquake. *Geophysical Research Letters*, *29*(8), 1238. https://doi.org/10.1029/2001GL014045

Ide, S., Baltay, A., & Beroza, G. (2011). Shallow dynamic overshoot and energetic deep rupture in the 2011 Mw 9.0 Tohoku-oki earthquake. *Science*, *332*(6036), 1426–1429. https://doi.org/10.1126/science.1207020

Igel, H., Djikpesse, H., & Tarantola, A. (1996). Waveform inversion of marine reflection seismograms for *P* impedance and Poisson's ratio. *Geophysical Journal International*, *124*, 363–371.

Jacob, J., Dyment, J., & Yatheesh, V. (2014). Revisiting the structure, age, and evolution of the Wharton Basin to better understand subduction under Indonesia. *Journal of Geophysical Research: Solid Earth*, *119*, 169–190. https://doi.org/10.1002/2013JB010285

Kamei, R., Pratt, R. G., & Tsuji, T. (2012). Waveform tomography imaging of a megasplay fault system in the seismogenic Nankai subduction zone. *Earth and Planetary Science Letters*. https://doi.org/10.1016/j.epsl.2011.10.042

Kerr, R. A. (2005). Model shows islands muted tsunami after latest Indonesian earthquake. *Science*, *308*, 341.

Kikuchi, M., Nakamura, M., & Yoshikawa, K. (2003). Source rupture process of the 1944 Tonankai earthquake and the 1945 Mikawa earthquake derived from low-grain seismograms. *Earth, Planets and Space*, *55*, 159–172.

Kitajima, H., & Saffer, D. M. (2012). Elevated pore pressure and anomalously low stress in regions of low frequency earthquakes along the Nankai Trough subduction megathrust. *Geophysical Research Letters*, *39*, L23301. https://doi.org/10.1029/2012GL053793

Knipe, R. J. (1992). Faulting processes and fault seal. In R. M. Larsen, H. Brekke, B. T. Larsen, & E. Talleraas (Eds.), *Structural and tectonic modelling and its application to petroleum geology, Norwegian Petroleum Society Special Publication, Proceedings of Norwegian Petroleum Society Workshop, 18–20 October 1989* (Vol. 1, pp. 325–342) Elsevier, Stavanger, Norway.

Kodaira, S., Iidaka, T., Kato, A., Park, J. O., Iwasaki, T., & Kaneda, Y. (2004). High pore fluid pressure may cause silent slip in the Nankai Trough. *Science*, *304*, 1295–1298.

Kodaira, S., Takahashi, N., Nakanishi, A., Miura, S., & Kaneda, Y. (2000). Subducted seamount imaged in the rupture zone of the 1946 Nankaido earthquake. *Science*, *289*, 104–106.

Kodaira, S., No, T., Nakamura, Y., Fujiwara, T., Kaiho, Y., Miura, S., et al. (2012). Coseismic fault rupture at the trench axis during the 2011 Tohoku-oki earthquake. *Nature Geoscience*, *5*(9), 646–650. https://doi.org/10.1038/NGEO1547

Konca, A. O., Avouac, J. P., Sladen, A., Meltzner, A. J., Sieh, K., Fang, P., et al. (2008). Partial rupture of locked patch of the Sumatra megathrust during the 2007 earthquake sequence. *Nature*, *456*(7222), 631–635. https://doi.org/10.1038/nature07572

Kopp, H., Hindle, D., Klaeschen, D., Oncken, O., Reichert, C., & Scholl, D. (2009). Anatomy of the western Java plate interface from depth-migrated seismic images. *Earth and Planetary Science Letters*, *288*, 399–407.

Korenaga, J., Holbrook, W. S., Singh, S. C., & Minshull, T. A. (1997). Natural gas hydrates on the southeast U.S. margin: Constraints from full waveform and travel time inversions of wide-angle seismic data. *Journal of Geophysical Research*, *102*, 15,345–15,365. https://doi.org/10.1029/97JB00725

Kristensen, T. B., Rotevatn, A., Peacock, D., Henstra, G. A., Midtkandal, I., & Grundvåg, S. A. (2016). Structure and flow properties of syn-rift border faults: The interplay between fault damage and fault-related chemical alteration (Dombjerg Fault, Wollaston Forland, NE Greenland). *Journal of Structural Geology*, *92*, 99–115.

Kuncoro, A. K., Cubas, N., Singh, S. C., Etchebes, M., & Tapponnier, P. (2015). Tsunamigenic potential due to frontal rupturing in the Sumatra locked zone. *Earth and Planetary Science Letters*, *432*, 311–322.

Ladage, S., Gaedicke, C., Barckhausen, U., Heyde, I., Weinrebe, W., Flueh, E. R., et al. (2006). Bathymetric survey images structure of Sumatra. *Eos, Transactions American Geophysical Union*, *87*(17), 165. https://doi.org/10.1029/2006EO170001

Lailly, P. (1983). The seismic inverse problem as a sequence of before stack migrations: Conference on Inverse Scattering, Theory and Application. Society of Industrial and Applied Mathematics, Expanded Abstracts, 206–220.

Lallemand, S. E., Schnurle, P., & Malavieille, J. (1994). Coulomb theory applied to accretionary and nonaccretionary wedges: Possible causes for tectonic erosion and/or frontal accretion. *Journal of Geophysical Research*, *99*, 12,033–12,055. https://doi.org/10.1029/94JB00124

Lauer, R. M., & Saffer, D. M. (2015). The impact of splay faults on fluid flow, solute transport and pore pressure distribution in subduction zones: A case study offshore the Nicoya Peninsula, Costa Rica. *Geochemistry, Geophysics, Geosystems*, *16*, 1089–1104. https://doi.org/10.1002/2014GC005638

Lay, T., Ammon, C. J., Kanamori, H., Yamazaki, Y., Cheung, K. F., & Hutko, A. R. (2011). The 25 October 2010 Mentawai tsunami earthquake (Mw 7.8) and the tsunami hazard presented by shallow megathrust ruptures. *Geophysical Research Letters*, *38*, L06302. https://doi.org/10.1029/2010GL046552

Lay, T., Kanamori, H., Ammon, C. J., Nettles, M., Ward, N. S., Aster, R. C., et al. (2005). The great Sumatra-Andaman earthquake of 26 December 2004. *Science*, *308*(5725), 1127–1133. https://doi.org/10.1126/science.1112250

Liu, C.-S., Curray, J. R., & McDonald, J. M. (1983). New constraints on the tectonic evolution of the eastern Indian Ocean. *Earth and Planetary Science Letters*, *65*(2), 331–342. https://doi.org/10.1016/0012-821X(83)90171-1

MacKay, M. E., Moore, G. F., Cochrane, G. R., Moore, J. C., & Julm, L. D. (1992). Landward vergence and oblique structural trends in the Oregon margin accretionary prism: implications and effect on fluid flow. *Earth and Planetary Science Letters*, *109*, 477–491.

McNeill, L. C., Dugan, B., Petronotis, K. E., Backman, J., Bourlange, S., Chemale, F., et al. (2017). Sumatra Subduction Zone. In *Proceedings of the International Ocean Discovery Program* (p. 362). College Station, TX: International Ocean Discovery Program. https://doi.org/10.14379/iodp.proc.362.103.2017

McNeill, L. C., & Henstock, T. J. (2014). Forearc structure and morphology along the Sunda subduction zone. *Tectonics*, *33*, 112–134. https://doi.org/10.1002/2012TC003264

Moeremans, R., Singh, S. C., Mukti, M., McArdle, J., & Johansen, K. (2014). Seismic images of structural variations along the deformation front of the Andaman-Sumatra subduction zone: Implications for rupture propagation and tsunamigenesis. *Earth and Planetary Science Letters*, *386*, 75–85.

Moore, G. F., Bangs, N. L., Taira, A., Kuramoto, S., Pangborn, E., & Tobin, H. J. (2007). Three-dimensional splay fault geometry and implications for tsunami generation. *Science*, *318*(5853), 1128–1131. https://doi.org/10.1126/science.1147195

Moore, J. C., & Saffer, D. M. (2001). Updip limit of the seismogenic zone beneath the accretionary prism of southwest Japan: an effect of diagenetic to low-grade metamorphic processes and increasing effective stress. *Geology*, *29*, 183–186.

Moore, J. C., & Vrolijk, P. (1992). Fluids in acretionary prisms. *Reviews of Geophysics*, *30*(2), 113–135. https://doi.org/10.1029/92RG00201

Mora, P. (1987). Nonlinear two-dimensional elastic inversion of multi-offset seismic data. *Geophysics*, *52*, 1211–1228.

Moser, T. J. (1991). Shortest path calculation of seismic rays. *Geophysics*, *56*, 59–67.

Natawidjaja, D. H., Sieh, K., Chlieh, M., Galetzka, J., Suwargadi, B. W., Cheng, H., et al. (2006). Source parameters of the great Sumatran megathrust earthquakes of 1797 and 1833 inferred from coral microatolls. *Journal of Geophysical Research*, *111*, B06403. https://doi.org/10.1029/2005JB004025

Ozawa, S., Nishimura, T., Suito, H., Kobayashi, T., Tobita, M., & Imakiire, T. (2011). Coseismic and postseismic slip of the 2011magnitude 9 Tohoku-Oki earthquake. *Nature*, *117*, 373–376. https://doi.org/10.1038/nature10227

Park, J.-O., Tsuru, T., Kaneda, Y., & Kono, Y. (1999). A subduction seamount beneath the Nankai accretionary prism off Shikoku, southwestern Japan. *Geophysical Research Letters*, *26*, 931–934.

Pica, A., Diet, J. P., & Tarantola, A. (1990). Nonlinear inversion of seismic reflection data in a laterally invariant medium. *Geophysics*, *55*, 284–292.

Prawirodirdjo, L., & Bock, Y. (2004). Instantaneous global plate motion model from 12 years of continuous GPS observations. *Journal of Geophysical Research*, *109*, B08405. https://doi.org/10.1029/2003JB002944

Qin, Y., & Singh, S. C. (2017). Detailed seismic velocity of the incoming subducting sediments in the 2004 great Sumatra earthquake rupture zone from full waveform inversion of long offset seismic data. *Geophysical Research Letters*, *44*, 3090–3099. https://doi.org/10.1002/2016GL072175

Romano, F., Trasatti, E., Lorito, S., Piromallo, C., Piatanesi, A., Ito, Y., et al. (2014). Structural control on the Tohoku earthquake rupture process investigated by 3D FEM tsunami and geodetic data. *Scientific Reports*, *4*(1), 5631. https://doi.org/10.1038/srep05631

Saffer, D. M., Silver, E. A., Fisher, A. T., Tobin, H., & Moran, K. (2000). Inferred pore pressures at the Costa Rica subduction zone: implications for dewatering processes. *Earth and Planetary Science Letters*, *177*, 193–207.

Saffer, D. M., & Tobin, H. J. (2011). Hydrogeology and mechanics of subduction zone forearcs: Fluid flow and pore pressure. *Annual Review of Earth and Planetary Sciences*, *39*, 157–186.

Shillington, D. J., Bécel, A., Nedimovi, M. R., Kuehn, H., Webb, S. C., & Abers, G. A. (2015). Link between plate fabric, hydration and subduction zone seismicity in Alaska. *Nature Geoscience*, *8*, 961–964.

Shipp, R., & Singh, S. C. (2002). Two-dimensional full wavefield inversion of wide-aperture marine seismic streamer data. *Geophysical Journal International*, *151*, 324–344.

Simons, M., Minson, S. E., Sladen, A., Ortega, F., Jiang, J., Owen, S. E., et al. (2011). The 2011 magnitude 9.0 Tohoku-Oki earthquake: Mosaicking the megathrust from seconds to centuries. *Science*, *332*(6036), 1421–1425. https://doi.org/10.1126/science.1206731

Singh, S. C., Carton, H., Tapponnier, P., Hananto, N. D., Chauhan, A. P. S., Hartoyo, D., & Bayly, M. (2008). Seismic evidence for broken oceanic crust in the 2004 Sumatra earthquake epicentral region. *Nature*. https://doi.org/10.1038/ngeo336

Singh, S. C., Hananto, N., Mukti, M., Permana, H., Djajadihardja, Y., & Harjono, H. (2011). Seismic images of the megathrust rupture during the 25th October 2010 Pagai earthquake, SW Sumatra: Frontal rupture and large tsunami. *Geophysical Research Letters*, *38*, L16313. https://doi.org/10.1029/2011GL048935

Singh, S. C., Hananto, N., Mukti, M., Robinson, D. P., Das, S., Chauhan, A., et al. (2011). Aseismic zone and earthquake segmentation associated with a deep subducted seamount in Sumatra. *Nature Geoscience*, *4*(5), 308–311. https://doi.org/10.1038/ngeo1119

Singh, S. C., Midenet, S., & Djajadihardja, Y. (2009). Seismic survey of the locked and unlocked Sumatra subduction zone. *Eos, Transactions American Geophysical Union*, *90*, 471.

Sugioka, H., Okamoto, T., Nakamura, T., Ishihara, Y., Ito, A., Obana, K., et al. (2012). Tsunamigenic potential of the shallow subduction plate boundary inferred from slow seismic slip. *Nature Geoscience*, *5*, 414–418. https://doi.org/10.1038/ngeo1466

Tanioka, Y., & Satake, K. (2001). Detailed coseismic slip distribution of the 1944 Tonankai earthquake estimated from tsunami waveforms. *Geophysical Research Letters*, *28*(6), 1075–1078. https://doi.org/10.1029/2000GL012284

Tarantola, A. (1984). Inversion of seismic reflection data in the acoustic approximation. *Geophysics*, *49*, 1259–1266.

Tarantola, A. (1986). A strategy for nonlinear elastic inversion of seismic reflection data. *Geophysics*, *51*, 1893–1903.

Tobin, H. J., & Saffer, D. M. (2009). Elevated fluid pressure and extreme mechanical weakness of a plate boundary thrust, Nankai Trough subduction zone. *Geology*, *37*, 679–682.

Tregoning, P., Brunner, F. K., Bock, Y., Puntodewo, S. S. O., McCaffrey, R., Genrich, J. F., et al. (1994). First geodetic measurement of convergence across the Java Trench. *Geophysical Research Letters*, *21*(19), 2135–2138.

Tsuji, T., Kamei, R., & Pratt, R. G. (2014). Pore pressure distribution of a mega-splay fault system in the Nankai Trough subduction zone: Insight into up-dip extent of the seismogenic zone. *Earth and Planetary Science Letters*, *396*, 165–178.

Tsuji, T., Tokuyama, H., Pisani, P. C., & Moore, G. (2008). Effective stress and pore pressure in the Nankai accretionary prism off the Muroto Peninsula, southwestern Japan. *Journal of Geophysical Research*, *113*, B11401. https://doi.org/10.1029/2007JB005002

Tudge, J., & Tobin, H. J. (2013). Velocity-porosity relationships in smectite-rich sediments: Shikoku Basin, Japan. *Geochemistry, Geophysics, Geosystems*, *14*, 5194–5207. https://doi.org/10.1002/2013GC004974

Ujiie, K., & Kimura, G. (2014). Earthquake faulting in subduction zones: Insights from fault rocks in accretionary prisms. *Progress in Earth and Planetary Science*, *1*(1), 1–30. https://doi.org/10.1186/2197-4284-1-7

Ujiie, K., Tanaka, H., Saito, T., Tsutsumi, A., Mori, J. J., Kameda, J., et al. (2013). Low coseismic shear stress on the Tohoku megathrust determined from laboratory experiments. *Science*, *342*(6163), 1211–1214. https://doi.org/10.1126/science.1243485

Van Avendonk, H. J. A., Shillington, D., Holbrook, W. S., & Hornbach, M. (2004). Inferring crustal structure in the Aleutian island arc from a sparse wide-angle seismic data set. *Geochemistry, Geophysics, Geosystems*, *5*, Q08008. https://doi.org/10.1029/2003GC000664

Virieux, J., & Operto, S. (2009). An overview of full waveform inversion in exploration geophysics. *Geophysics*, *74*, WCC127–WCC152.

Von Huene, R., Ranero, C. R., & Vannucchi, P. (2004). Generic model of subduction erosion. *Geology*, *32*, 913–916. https://doi.org/10.1130/G20563.1.

Vrolijk, P., Fisher, A., & Gieskes, J. (1991). Geochemical and geothermal evidence for fluid migration in the Barbados accretionary prism (ODP leg 110). *Geophysical Research Letters*, *18*, 947–950. https://doi.org/10.1029/91GL00913

Wei, S., Graves, R., Helmberger, D., Avouac, J. P., & Jiang, J. (2012). Sources of shaking and flooding during the Tohoku-Oki earthquake: A mixture of rupture styles. *Earth and Planetary Science Letters*, *333–334*, 91–100.

White, R. S., McKenzie, D., & O'Nions, R. K. (1992). Oceanic crustal thickness from seismic measurements and rare earth element inversions. *Journal of Geophysical Research*, *97*, 19,683–19,715. https://doi.org/10.1029/92JB01749

Zelt, B. C., Ellis, R. M., Clowes, R. M., & Hole, J. A. (1996). Inversion of three-dimensional wide-angle seismic data from the southwestern Canadian Cordillera. *Journal of Geophysical Research*, *101*, 8503–8529. https://doi.org/10.1029/95JB02807

Zelt, C. A. (1998). Lateral velocity resolution from three-dimensional seismic refraction data. *Geophysical Journal International*, *135*, 1101–1112.

Zelt, C. A., Hojka, A. M., Flueh, E. R., & McIntosh, K. D. (1999). 3D simultaneous seismic refraction and reflection tomography of wide-angle data from the central Chilean margin. *Geophysical Research Letters*, *26*, 2577–2580. https://doi.org/10.1029/1999GL900545

Zhang, J., & Toksöz, M. N. (1998). Nonlinear refraction traveltime tomography. *Geophysics*, *63*, 1726–1737.